Large-Eddy Simulation (LES) for Airfoils Static and Dynamic Stall using One-equation SGS Model based on Dynamic Procedure

MOHAMAD FIRDAUS BIN

January 2021

Graduate School of Engineering

OSAKA UNIVERSITY

Abstract

The objective of this study is to develop a practical method of the large-eddy simulation (LES), especially for the analysis of flow around an airfoil in unsteady motion. LES is the computational method for turbulent flows, and it has been widely applied in the industry. In LES, the unsteady motion of the scale larger than the computational grid is directly solved, while the smaller scale motion is given by the theoretical model, that is, the subgrid scale (SGS) model. It is still difficult to predict laminar-turbulent transition and flow separation even by sophisticated SGS models. In addition, the universal law of the wall has not been established, and, as a result, resolving the turbulent boundary layer becomes costly. The flow around an airfoil is a typical example of these difficulties, namely laminar separation in a static condition and massive separation that causes a dynamic stall in a pitching motion.

In this study, the one-equation dynamic (OD) model was introduced to simulate the flows around an airfoil in a static condition and pitching motion. The SGS eddy viscosity was parameterized using SGS kinetic energy, which was estimated by the transport equation. The OD model determined the production term in the transport equation using the dynamic Smagorinsky model through the Germano procedure. Owing to these formulations, it could deal with nonequilibrium feature of spatially developing flow and two-way energy transfer between resolved and SGS portions. By implementing the OD model into a practically arranged grid on general curvilinear coordinates, static and dynamic stalls of airfoils were reproduced. In a flow around an 'A-profile' airfoil at rest, it was proven that the SGS eddy viscosity turned to zero in the laminar region and the observed transition point was in good agreement with the experimental data. Then the procedure of laminar separation, reattachment, and transition to turbulence was successfully reproduced with relatively lower computational cost in comparison with the previous methods considered in the LESFOIL project. Furthermore, the OD model was applied for the flow around a NACA0012 airfoil in sinusoidally pitching motion. As a result, the essential characteristics including the laminar separation bubble (LSB), reattachment, leading-edge vortex (LEV), trailing-edge vortex (TEV), and dynamic stall vortex (DSV) were observed. The angles of LSB and LEV onsets were in good agreement with the experimental observation.

The result of this study revealed that the OD model was able to predict a wide variety of flow physics involved in static and dynamic stalls without any additional transition model and with practical computational capacity.

Acknowledgements

Firstly, I would like to express my sincere gratitude to my advisor Prof. Takeo KAJISHIMA for the continuous support of my Ph.D. study, for his patience, motivation, and immense knowledge. His guidance helped me in all the time of research and writing of this thesis. I hope that one day, I could be as lively, enthusiastic, and energetic as him.

I am also thankful to Prof. Toshitsugu TANAKA and Prof. Takeru YANO for their time and valuable advice to complete the thesis. My sincere thanks also go to Dr. Shintaro TAKEUCHI, Dr. Takeshi OMORI, and Dr. Kie OKABAYASHI, for their valuable knowledge sharing and help during my 3-year journey in Osaka. Without their precious support, it would not be possible to conduct this research. I also would like to express my thanks to all the staff and members of the laboratory, especially Shugo KIMURA, Yuri MIYAMORI, and Masahiro ADACHI; without their help, I could not complete my study.

To my wife, Sahlizal, there are no words to describe my love and thanks to you. You have been supportive, caring, and understanding throughout my Ph.D. journey.

I gratefully acknowledge the funding received towards my Ph.D. from the Ministry of Higher Education (MOHE) Malaysian and Universiti Teknologi MARA (UiTM).

Contents

List of Figures

List of Abbreviations and Symbols

Abbreviations

LES	Large-eddy simulation
SGS	Subgrid Scale
GS	Grid scale
OD	One-equation Dynamic Model
LEV	Leading-edge Vortex
DSV	Dynamic Stall Vortex
TEV	Trailing-edge Vortex
NSE	Navier-Stokes Equation
SLV	shear-layer vortex
SM	Smagorinsky Model
DSM	Dynamic Smagorinsky Model
RAST	Rahman–Agarwal–Siikonen–Taghinia
LSB	Laminar separation bubble
DNS	Direct numerical simulation
MTS	Mixed time scale
QUICK	Quadratic upstream interpolation for convective kinematics
SOR	Successive over-relaxation
CFL	Courant–Friedrichs–Lewy
ILES	Implicit large-eddy simulation
URANS	Unsteady Reynolds Average Navier-Stokes
SST	Shear stress transport

Symbols

Re_c	Reynolds number based on chord length
k	Turbulent kinetic energy
k_t	Total turbulent kinetic energy

ν_t	Turbulent viscosity
C	chord length
U_∞	freestream velocity
G	Grid filter function
$\bar{u}_i$	Grid filter velocity
$\bar{D}_{ij}$	Grid-scale rate-of-strain tensor
τ_{ij}	Sub-grid-scale stress
ρ	Density
$\bar{\Delta}$	Grid filter length
C_v	Eddy viscosity coefficient
L_{ij}	Germano identity
$\tilde{\bar{u}}_i$	Test filter velocity
α	Test filter ratio
ε_ω	Additional dissipation
C_ε	Dissipation coefficient
J	Jacobian
γ^{kl}	Symmetric tensor
y^+	Dimensionless wall distance, $\frac{yU_\tau}{\nu}$
U_τ	Wall friction velocity
C_D	Drag Coefficient
C_L	Lift Coefficient
C_P	Pressure Coefficient
C_f	Skin friction coefficient
τ_ω	Wall shear stress
Ω'_i	Angular velocity component of the non-inertial system
ϵ_{ijk}	Levi-Civita's alternating tensor
α_{mean}	mean angle of attack
α_{amp}	Amplitude angle
α_{min}	Minimum angle of attack
α_{max}	Maximum angle of attack

↑	Upstroke motion
↓	Downstroke motion

CHAPTER 1

Introduction

1.1 Background

Prediction of complex flow fields involving both static and dynamic stall is important in a broad range of industrial applications such as turbomachinery, wind turbine aerodynamics, helicopter blade rotors, and maneuverable wings. Variations of flow phenomena such as laminar, transition, flow separation, and development of vortex around the airfoil have been studied numerically by many researchers to understand the flow physics for each phenomenon. These complex flow fields are different from the static and dynamic stall points of view. In a static or steady pitch airfoil, the complex flow fields near the stall angle consist of laminar separation, flow reattachment, and flow separation near the trailing edge. Hence, capturing all the flow phenomena is essential to obtain a good and accurate aerodynamics load such as drag, lift, and moment coefficient. While for the dynamic stall, the development of various vortex such as leading-edge vortex (LEV), dynamic stall vortex (DSV), and trailing edge vortex (TEV) are vital for dynamic stall process. Besides, vortex shedding is also part of an important flow mechanism in dynamic stall regions.

1.2 Static Stall Simulation

One of the case studies that focus on the complex flow around an airfoil near stall angle is the A-profile airfoil (Figure 1). The flow around A-profile airfoil (A-airfoil) at an angle of attack 13.3° and Reynolds number based on chord length and freestream velocity Re_c=2.1 × 10^6 has been used as a case study in this thesis. Established experimental results from an ONERA wind tunnel revealed a complex flow configuration that involved the laminar-transition region, reattachment, and trailing edge separation. These flow configurations have been studied extensively via large-eddy simulations (LES) by a group of researchers in a LESFOIL project

[1]. Their study focused on different types of grid arrangements, numerical approach, and the effect of SGS models.

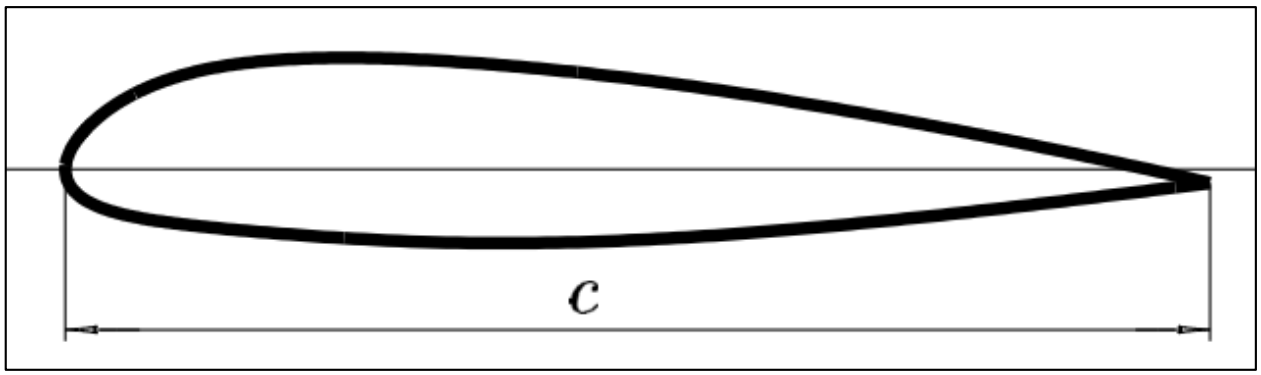

Figure 1-1 A-profile Airfoil.

Complex flow phenomena over the A-airfoil have offered different complexities to resolve all the important flow structures in large-eddy simulations (LES). Both grid arrangement and SGS models play important roles in capturing the flow structures. Mary and Sagaut [1] revealed in their LESFOIL report the importance of fine grid resolution for the better solution accuracy of pressure coefficient compared to that obtained from the subgrid scale (SGS) models. On the other hand, they also concluded that the explicit SGS model managed to capture the important flow structures if the grid was sufficiently fine [1]. Even though the work from Mary and Sagaut was remarked as the most successful result in a LESFOIL project, their grid arrangement method on the region of flow interest may not be a universal method. In 2018, Asada and Kawai revisited the LESFOIL project and their results, with more than 1200 million nodes, displayed a perfect agreement with the experimental data [2].

As far as engineering applications are concerned, billions of grid numbers over the flow of interest are not practical approaches despite the great success of Asada and Kawai [2]. Their method also needs prior information about the flow configuration, such as transition and separation point, which is not a universal approach if that information is not on hand. Dahlstrom and Davidson [3] applied a numerical treatment for the laminar and transition region where a bounded second-order upwind scheme was used to remove the unphysical oscillations around the leading edge. Treatment of SGS model was also implemented upstream of the transition region where the SGS turbulent kinetic energy k_{SGS} was set to zero. Despite all these treatments, the transition point results were still far downstream and upstream of the exact transition point

[3]. Later, they improved the grid resolution in a streamwise direction, and as a result, there was SGS dissipation in the laminar region even though a similar treatment was applied [4].

For a complex flow around an airfoil, the laminar-transitional flow region is an important phenomenon that requires a fair and accurate prediction. The laminar separation bubble (LSB) initiated from the separated shear layer is also visible in this region. In the laminar region, no turbulent kinetic energy should have appeared. Therefore, the turbulence model's selection that can sense the laminar region should be employed in the simulation. Previous work by Mary and Sagaut [1] refined the grid resolution in the laminar-transition region. On top of that, they also set the eddy viscosity, ν_t to zero upstream of the transition points. Dahlstrom and Davidson [4] performed a similar method, whereas the production term in one-equation k_{SGS} was set to zero in the range of 15% from the leading edge. However, their approach is less significant, where they have discovered that the total turbulent kinetic energy has also appeared in the laminar region.

Based on the eddy viscosity model of Smagorinsky, the rate of strain tensor and filter width are always non-zero. Therefore, it is almost impossible to obtain zero eddy viscosity in the non-turbulent region. However, the Smagorinsky constant can become zero if it is calculated locally and instantaneously varying in space and time. The dynamic procedure is known as an effective method to determine the coefficient locally for LES. This procedure was first proposed by Germano et al. [5] and later improved by Lilly [6] to solve the drawbacks of the constant eddy viscosity coefficient in the Smagorinsky Model (SM). Later, the dynamic procedure was also incorporated to determine the coefficient in the transport equation of k_{SGS}. Ghosal et. al [7] stressed the importance of tracing the energy in subgrid scale which allowed for the transfer of energy from subgrid scale to resolve scale or energy backscatter. They allowed for the negative sign of coefficient calculated through the transport equation of subgrid scale kinetic energy and made the eddy viscosity depended on the subgrid scale kinetic energy k_{SGS}.

The purpose of this investigation is to evaluate the capability of the OD model to reproduce the flow physics around the laminar region with a smaller number of grid points. The feature of the OD model is to remove the artificial treatments in the laminar-transition region. The author believes that the effect of turbulent kinetic energy transfer from GS to SGS is best defined through the production term of k_{SGS} transport equation. This model is different from others in

terms of defining the production term. Further explanation of this model is described in Chapter 2.

1.3 Dynamic Stall Simulation

Dynamic stall is defined as the phenomenon of exceeding the normal static stall angle. This phenomenon is associated with various complex fluid flows such as separations, reattachments, and vortex developments, which contribute to the unusual aerodynamic characteristics. In terms of turbulence interactions, the dynamic stall produces strong nonequilibrium turbulence in which the turbulence kinetic energy production is imbalanced with the dissipation [8]. Therefore, common SGS turbulence models are thought to be insufficient to correctly capture the drastic changes of aerodynamic loads at high angles of attack and moderately high Reynolds numbers.

Experimental works are required to understand and visualize the phenomena of oscillating airfoils. McCroskey et al. [9] conducted an experiment based on oscillating NACA0012 airfoil by using a 7 × 10 ft wind tunnel to investigate the boundary layer separation and vortex shedding mechanism. They concluded that the unsteady separation of the turbulent boundary layer was the primary cause of the vortex shedding mechanism. In addition, Lee and Gerontakos [10] executed several experiments to understand the overall flow phenomena of dynamics stall around an oscillating airfoil. They revealed a clear mechanism of the dynamic stall at different stages, such as light-stall oscillating and attached-flow oscillating cases.

Additionally, computational simulations are crucial for any fluid flows analysis. For the dynamic stall simulations, the unsteadiness of boundary layer interaction induced by oscillation can be captured and visualized by means of numerical simulations. Since boundary layer interaction is involved, very fine grid density is required to capture all the vortices for the entire dynamic stall process which includes unsteady boundary layer separation, transition, shear layer instabilities, laminar separation bubble (LSB) bursting, and vortex surface interactions [11], [12]. Thereby, Direct Numerical Simulation (DNS) is a more suitable solution if the computational resources are not a problematical issue. However, as the Re number increases especially for industrial engineering applications such as helicopter blade rotors, wind turbine blades, and maneuverable wings [11], [13], the DNS demands huge computational capability and memory space. Hence the Reynolds-averaged Navier-Stokes (RANS) also can be considered as an option. However, some researchers claim that RANS has to be accompanied by transitional models to correct some deficiencies [11], [14].

Large-eddy simulation (LES) has gained more attention in studying the complexity of dynamic stall phenomena. A series of comprehensive dynamic stall simulations using LES can be reviewed in Visbal and Garmann [15], Benton and Visbal [16], Visbal and Benton [11], and Visbal [17]. However, none of these studies focused on the effect of nonequilibrium of turbulence models. Dindart and Kaynak [18] revealed the importance of a nonequilibrium SGS model to determine the separation and vortex shedding mechanism of the dynamic stall compared to an equilibrium SGS model. A study by Mukai et al. showed that the LES of the Smagorinsky model (SM) with coarse grid spacing in the spanwise direction successfully captured some aspects of the unsteady phenomenon [19], [20]. Gulillaud et al. [21] also used SM to study the effect of the leading edge vortex (LEV) on the lift coefficient unsteadiness on a pitching NACA0012 at a Reynolds number of 20000.

Meanwhile, a Mixed-Time-Scale (MTS) SGS model was used by Almutairi et al. [22] to observe the laminar separation bubbles (LSB) near stall of NACA0012 at a Reynolds number of 5×10^4. They reported that an increase of the spanwise domain contributed to intermittent bursting of the laminar separation bubble. Wang et al. [23] used four equations model where the k-ε model was coupled with the shear stress transport (SST) model in order to capture the LSB. They revealed that the angle onset for the LSB was in good agreement with the experimental observation. In addition, Kim and Xie [24] also investigated the dynamic stall of NACA0012 using the MTS model to have a better understanding of several factors such as spanwise extension and the effect of freestream turbulence.

For the second objective, the author aims to understand the large-scale unsteady motions of an airfoil in deep dynamic stall events. The focus is to investigate further the OD model's capability to predict leading-edge transitional flow in unsteady pitching mode. As stated in the literature, most of the simulations, such as Unsteady Reynolds Average Navier-Stokes (URANS), require an additional transitional model to correct the leading-edge transitional region's flow behavior. For the unsteady pitching airfoil, the leading-edge transitional flow promotes a significant role in the development of downstream flow such as separation, dynamic stall vortex, and trailing edge vortex.

1.4 Concluding Remarks

In this chapter, the current status of the method to predict the laminar-transition region was reviewed, and a special treatment to switch between the laminar and turbulent region was

discovered to solve the issue. This special treatment required the physical characteristic such as the transition point in hand, and the SGS eddy viscosity and k_{SGS} were set to zero in that region. For sinusoidal pitching airfoil, the leading-edge transitional region such as the LSB was the essential phenomenon to be captured in the simulations. The transition model, such as the SST model coupled with the k-ε model, predicted the LSB with the correct onset angle. For the LES, a full 3D simulation with a one-equation k_{SGS} model is still uncovered for the dynamic stall simulation.

CHAPTER 2

Governing Equations

2.1 Basic Equation for LES

This simulations were based on the filtered Navier-Stokes equations for incompressible flow where all the variables were non-dimensionalized by the chord length C, and the freestream velocity U_∞. Low pass filtering based on the spatial filter was used to differentiate between resolvable scale (large) and unresolvable scale (small). The filtering operation is represented as

$$\bar{f}(x) = \int_{-\infty}^{\infty} G(y) f(x-y)\, dy, \tag{2-1}$$

where G is the "grid filter" function having the representative length corresponding to the width of the computational grid. The filtered continuity and momentum equations are

$$\frac{\partial \bar{u}_i}{\partial x_i} = 0, \tag{2-2}$$

$$\frac{\partial \bar{u}_i}{\partial t} + \frac{\partial}{\partial x_j}\left(\overline{u_i u_j}\right) = -\frac{1}{\rho}\frac{\partial \bar{p}}{\partial x_i} + \frac{\partial}{\partial x_j}\left(2\nu \bar{D}_{ij}\right). \tag{2-3}$$

Equation 2-3 contains a nonlinear term $\left(\overline{u_i u_j}\right)$ which cannot be resolved by the grid scale (GS) variables. Hence, rewriting the equation 2-3

$$\frac{\partial \bar{u}_i}{\partial t} + \frac{\partial}{\partial x_j}\left(\bar{u}_i \bar{u}_j\right) = -\frac{\partial \bar{P}}{\partial x_i} + \frac{\partial}{\partial x_j}\left[2\nu \bar{D}_{ij} - \tau_{ij}\right], \tag{2-4}$$

where $\bar{D}_{ij}$ is the grid-scale rate-of-strain tensor

$$\bar{D}_{ij} = \frac{1}{2}\left(\frac{\partial \bar{u}_i}{\partial x_j} + \frac{\partial \bar{u}_j}{\partial x_i}\right). \tag{2-5}$$

Equation 2-4 consists of $\bar{u}_i$ which is denoted as the GS component of velocity, $\bar{P} = \bar{p}/\rho$ is the GS component of pressure, ρ is the fluid density, and ν is the kinematic viscosity of fluid. Term τ_{ij} is known as the residual stress or subgrid scale (SGS) stress. This term consists of unresolved stress, which needs to be modeled.

$$\tau_{ij} = \overline{u_i u_j} - \bar{u}_i \bar{u}_j \qquad 2\text{-}6$$

2.2 Subgrid Scale (SGS) Models

In order to solve the equation of motion in Eq. 2-4, the τ_{ij} needed to be modeled. The approximation of τ_{ij} was based on the Boussinesq approximation where the unresolved scales in the turbulent flow was solved by means of the eddy viscosity model, ν_t and can be defined as

$$\tau_{ij} = -2\nu_t \bar{D}_{ij} + \frac{1}{3}\tau_{kk}\delta_{ij}. \qquad 2\text{-}7$$

The first SGS model is known as the Smagorinsky model. This model was proposed by Smagorinsky in 1973. The main idea for this model is based on the local equilibrium assumption made between production and dissipation. In other words, the energy produced from resolved scales is equal to the energy dissipation on unresolved scales. The Smagorinsky Model (SM) is described as

$$\nu_t = (C_S \bar{\triangle})^2 |\bar{D}| \qquad 2\text{-}8$$

where C_S is known as the Smagorinsky constant. The grid filter width, $\bar{\triangle}$ can be calculated based on the cell volume

$$\bar{\Delta} = \sqrt[3]{\Delta_1 \Delta_2 \Delta_3}\,. \qquad 2\text{-}9$$

and $|\bar{D}|$ is defined as the norm of strain rate tensor for resolved scales

$$|\bar{D}| = \sqrt{2\bar{D}_{ij}\bar{D}_{ij}}\,. \qquad 2\text{-}10$$

A constant global value is set for the C_S in Eq. 2-8. The constant can be modified, such as 0.1 for channel flow, 0.12 – 0.14 for mixing-layer flow, and 0.23 in decaying turbulence [25]. Therefore, one of the shortcomings of the SM is related to the non-universal value of the constant. Besides, the SM also needs a damping function of Van Driest's type to correct the behavior near the wall. On top of that, the SM is unable to remove the SGS eddy viscosity in the laminar region. Despite all the shortcomings, the SM is known as one of the LES's most popular models due to its robustness and simplicity.

The shortcoming of defining the C_S in SM was solved by Germano in 1991. Based on his idea, the constant in SM is calculated dynamically, varying in space and time. The method is

known as a dynamic approach, and the model is called Dynamic Smagorinsky Model (DSM). In order to execute the dynamic procedure, another filter is introduced, which is known as a test filter (denoted throughout this work by $\tilde{.}$), and $\widetilde{\Delta}$ is defined as a test filter width. The function of the test filter is to filter the smallest scale left in the resolved scales. Normally, the test filter width is set greater than the grid filter width, and the ratio between these two filters is denoted as α. The Germano identity reads

$$L_{ij} = T_{ij} - \tilde{\tau}_{ij} = \left(\widetilde{\overline{u_i}\overline{u_j}} - \tilde{\bar{u}}_i\tilde{\bar{u}}_j\right) - \left(\widetilde{\overline{u_i}\overline{u_j}} - \widetilde{\bar{u}_i}\widetilde{\bar{u}_j}\right) = \widetilde{\overline{u_i}\overline{u_j}} - \tilde{\bar{u}}_i\tilde{\bar{u}}_j \qquad 2\text{-}11$$

where T_{ij} is the SGS stress on the test filter level. Another parameter associated with the dynamic procedure is

$$M_{ij} = \alpha^2\left|\widetilde{\bar{D}}\right|\widetilde{\bar{D}}_{ij} - \widetilde{|\bar{D}|\bar{D}}_{ij}. \qquad 2\text{-}12$$

Based on these two tensors, the Smagorinsky constant C_S, can be computed as

$$c = -\frac{1}{2\bar{\Delta}^2}\frac{L_{ij}M_{ij}}{M_{kl}M_{kl}}. \qquad 2\text{-}13$$

The SM is developed based on the local equilibrium principal between production and dissipation. However, the flow associated with high Reynolds number flows or separated flows is far from the equilibrium assumption. Based on this argument, another type of SGS model is developed based on the SGS turbulent kinetic energy, $k_{SGS} = \frac{1}{2}\left(\overline{u_k u_k} - \bar{u}_k\bar{u}_k\right)$, and this model is known as the One-equation model. The first one-equation model was theoretically derived by Yoshizawa and Horiuti [26] in 1985. The transport equation of k_{SGS} is derived as

$$\frac{\partial k_{sgs}}{\partial t} + \frac{\partial}{\partial x_j}\left(\bar{u}_j k_{sgs}\right) = P_{k_{sgs}} - C_\varepsilon\frac{k_{sgs}^{\frac{3}{2}}}{\bar{\Delta}} + \frac{\partial}{\partial x_j}\left[\frac{\nu_t}{\sigma_k}\frac{\partial k_{sgs}}{\partial x_j}\right] \qquad 2\text{-}14$$

where the production, dissipation, and diffusion appear on the right-hand side of the transport equation. The production term is defined as $P_{k_{sgs}} = -\tau_{ij}\bar{D}_{ij}$ where the SGS stress is calculated based on

$$\tau_{ij} - \frac{2}{3}k_{SGS}\delta_{ij} = -2\nu_t\bar{D}_{ij}. \qquad 2\text{-}15$$

The eddy viscosity that accounted for the dissipation of SGS is calculated as $\nu_t = C_k\bar{\Delta}\sqrt{k_{sgs}}$. A similar eddy viscosity equation is utilized for the production term.

2.3 One-Equation Dynamic Model (OD)

In 1999, a modified version of the one-equation transport equation was proposed by Okamoto and Shima [27]. This version was fundamentally similar to Eq. 2-14; however, an additional dissipation term was added to consider near-wall turbulence solution [28]. Meanwhile, the diffusion term also includes the ν rather than only ν_t. The k_{SGS} transport equation is now

$$\frac{\partial k_{SGS}}{\partial t}+\frac{\partial}{\partial x_j}\left(\bar{u}_j k_{SGS}\right)==-\tau_{ij}\bar{D}_{ij}-C_\varepsilon\frac{k_{SGS}^{\frac{3}{2}}}{\bar{\Delta}}-\varepsilon_\omega+\frac{\partial}{\partial x_j}\left[\left(\nu+C_d\Delta_v\sqrt{k_{SGS}}\right)\frac{\partial k_{SGS}}{\partial x_j}\right], \tag{2-16}$$

where the additional term, ε_ω is calculated as

$$\varepsilon_\omega=2\nu\frac{\partial\sqrt{k_{SGS}}}{\partial x_j}\frac{\partial\sqrt{k_{SGS}}}{\partial x_j}. \tag{2-17}$$

The SGS eddy viscosity is expressed differently from the previous version

$$\nu_t=C_v\Delta_v\sqrt{k_{SGS}} \tag{2-18}$$

where C_v is set equal to 0.05. Here, the coefficient C_v is different from C_k in previous SGS eddy viscosity. The characteristic length, Δ_v is given as [27]

$$\Delta_v=\frac{\bar{\Delta}}{1+\frac{C_k\bar{\Delta}^2\bar{D}^2}{k_{SGS}}} \tag{2-19}$$

where $C_k=0.08$.

Various studies [7], [29]–[31] have utilized similar eddy viscosity that is used in the equation of motion to define the SGS stress, τ_{ij} in the production term (first term on right hand side of Eq. 2-16). Inagaki and Abe [32] stressed the difficulty of predicting the physical flow phenomena if $\sqrt{k_{SGS}}$ and the grid filter width were utilized in the production term. This is evident when most of the flows involved in engineering applications are normally accompanied by the laminar and turbulent region. A previous study by Dahlstrom and Davidson [4], for instance, showed that the k_{SGS} appeared in the laminar region.

In this work, the production term was defined differently from the other previous versions of one-equation k_{SGS}. The SGS stress in production term was calculated using the DSM. By implementing the DSM, this model used two different SGS eddy viscosity whereby Eq. 2-18 was used in the equation of motion, while Eq. 2-8 was utilized for the production term. The coefficient in the DSM was determined dynamically that allowed a clearer representation of flow phenomena. Based on the DSM explained in the previous section, the coefficient was

calculated by using Eq. 2-13 in which the calculation was mainly based on the results of the filtering process from the GS. Several dynamic procedures have been introduced by Ghosal et al. [7] and Davidson [33] to determine the coefficient in one-equation k_{SGS}. However, their dynamic version is used to calculate the coefficient in dissipation term C_ε and C_k in SGS eddy viscosity equation.

Kajishima and Nomachi [34] named this approach as the One-equation dynamic model (OD). Their approach defined the production term as

$$P_{k_{SGS}} = -\tau_{ij}\overline{D}_{ij} = 2(c\bar{\Delta}^2|\overline{D}|)\overline{D}_{ij}\overline{D}_{ij} = c\bar{\Delta}^2|\overline{D}|^3. \qquad 2\text{-}20$$

The dynamic procedure of DSM was used to obtain the coefficient, c. In this work, any smoothing or averaging was not necessary, and thus a negative value of c by Eq. 2-13 was allowed. The negative value indicated the reverse transfer of energy or from SGS to GS portion, which was important for inhomogeneous cases. It is important to note that the negative value of the production term would only decrease the k_{SGS}. The backscatter of energy was not represented in the filtered equation of motion because the eddy viscosity v_t was always positive. Furthermore, the advantage of removing the averaging and smoothing would also make the OD model more flexible for engineering interest in the absence of homogeneous directions. For the energy losses or dissipation, Eq. 2-18 was adopted. The effect of SGS diffusion was accounted for in the last term of Eq. 2-16. The constant-coefficient for the dissipation term was set as 0.835, as recommended by Okamoto and Shima [27].

2.4 Concluding Remarks

This chapter intends to provide a general outline of how the OD model was derived. The one-equation k_{SGS} model was shown, and each term in the transport equation was explained. The idea of calculating the production term based on the DSM was emphasized. Owing to these formulations, it could deal with the nonequilibrium feature of spatially developing flow and two-way energy transfer between resolved and SGS portions.

CHAPTER 3

Application of the OD Model in Static Stall Simulation

3.1 Generalized Coordinate System

In chapter 2, the Navier-Stokes equations were defined in terms of the Cartesian coordinate system. The transformation from the Cartesian coordinate system to the general curvilinear coordinate system is shown here. Eq. 2-2 and 2-4 are rewritten as

$$\frac{1}{J}\frac{\partial(J\bar{U}^k)}{\partial\xi^k} = 0, \tag{3-1}$$

$$\frac{\partial\bar{u}_i}{\partial t} + \frac{1}{J}\frac{\partial(J\bar{U}^k\bar{u}_i)}{\partial\xi^k} + \frac{1}{J}\frac{\partial}{\partial\xi^k}\left[J\frac{\partial\xi^k}{\partial x_i}\left(\bar{P} + \frac{2}{3}k_{SGS}\right)\right] = \frac{1}{J}\frac{\partial}{\partial\xi^k}\left[J\frac{\partial\xi^k}{\partial x_i}(\sigma_{ij})\right], \tag{3-2}$$

where

$$\sigma_{ij} = 2(\nu + \nu_t)\left(\bar{D}_{ij} - \tfrac{1}{3}\bar{D}_{kk}\right). \tag{3-3}$$

Then, the transformation of Grid-scale rate-of-strain tensor in eq. 2-5 is

$$\bar{D}_{ij} = \frac{1}{2}\left(\frac{\partial\xi^l}{\partial x_i}\frac{\partial\bar{u}_i}{\partial\xi^l} + \frac{\partial\xi^l}{\partial x_j}\frac{\partial\bar{u}_j}{\partial\xi^l}\right). \tag{3-4}$$

The Jacobian, J of the coordinate transformation is defined as

$$J = \begin{vmatrix} x_\xi & x_\eta & x_\zeta \\ y_\xi & y_\eta & y_\zeta \\ z_\xi & z_\eta & z_\zeta \end{vmatrix}, \quad \frac{1}{J} = \begin{vmatrix} \xi_x & \xi_y & \xi_z \\ \eta_x & \eta_y & \eta_z \\ \zeta_x & \zeta_y & \zeta_z \end{vmatrix}. \tag{3-5}$$

The transformation between the velocity components can be expressed as

$$\bar{U}^k = \frac{\partial\xi^k}{\partial x_i}\bar{u}_i, \qquad \begin{bmatrix} U \\ V \\ W \end{bmatrix} = \begin{vmatrix} \xi_x u + \xi_y v + \xi_z w \\ \eta_x u + \eta_y v + \eta_z w \\ \zeta_x u + \zeta_y v + \zeta_z w \end{vmatrix}. \tag{3-6}$$

The transport equation of k_{SGS} is also transformed into a curvilinear coordinate system where Eq. 2-16 is transformed as

$$\frac{\partial k_{sgs}}{\partial t}+\frac{1}{J}\frac{\partial}{\partial \xi^k}\left(J\bar{U}^k k_{sgs}\right)=P_{k_{sgs}}-C_\varepsilon\frac{k_{sgs}^{\frac{3}{2}}}{\bar{\Delta}}-\varepsilon_\omega+\frac{1}{J}\frac{\partial}{\partial \xi^k}\left[\left(\nu+C_d\Delta_v\sqrt{k_{sgs}}\right)\gamma^{kl}\frac{\partial k_{sgs}}{\partial \xi^l}\right], \quad 3\text{-}7$$

where γ^{kl} is known as a symmetric tensor.

$$\gamma^{kl}=J\frac{\partial \xi^k}{\partial x_m}\frac{\partial \xi^l}{\partial x_m}. \quad 3\text{-}8$$

The additional dissipation term, ε_ω is also transformed into

$$\varepsilon_\omega=2\nu\left(\frac{\partial \xi^k}{\partial x_j}\frac{\partial\sqrt{k_{sgs}}}{\partial \xi^k}\right)\left(\frac{\partial \xi^l}{\partial x_j}\frac{\partial\sqrt{k_{sgs}}}{\partial \xi^l}\right). \quad 3\text{-}9$$

3.2 Numerical Method and Computational Setup

In the present simulation, spatially filtered incompressible Navier-Stokes equations (NSE) were discretized based on the finite difference method by using the in-house code. The diffusion terms in NSE were discretized by the 2nd order central finite difference, while the quadratic upstream interpolation for convective kinematics (QUICK) method was applied to the convective terms. The QUICK method has an advantage in numerical stability for the simulation of high Re number flows and has been proven in [35]. For the transport equation of k_{SGS}, the nonlinear term was solved based on the donor-cell method procedure.

The time marching to solve the viscous and convective terms was based on the explicit Adams-Bashforth method of the 2nd order accuracy. Besides, this method was also used to solve the time marching in the transport equation of k_{SGS}. The pressure Poisson equation was solved using Successive Over-Relaxation (SOR). The computational time step was set as $3.0\times10^{-5}c/U_\infty$, giving the maximum CFL number of around 0.2.

Computational conditions used in this simulation corresponded to those experiments conducted at the ONERA F1 wind tunnel where the angle of attack was 13.3°, the Reynolds number based on the chord length C and freestream velocity U_∞, and Re_c $(=\frac{CU_\infty}{\nu})=2.1\times10^6$. In order to observe the effects of the OD model, a similar computational setup performed by Dahlstrom and Davidson [3], in terms of grid number, was used. The essential difference between our computational setup and Dahlstrom and Davidson [3] was the method of handling the eddy viscosity in the laminar region, where they used an artificial approach by setting the eddy viscosity to zero in the laminar region. Apart from that, the mesh used in their simulation was refined in the transition region to capture the laminar-transition phenomena. In our method,

no artificial approaches were performed, which allowed the checking of the OD model's capability.

In the x-y plane, the so-called *C*-grid was generated where ξ coordinate went around the airfoil and η was in the outward direction from the solid wall and cut-line after the trailing edge. Meanwhile, ζ was in the spanwise direction. The domain was extended up to 20*C* (20 times of the chord length) in both the X-direction and Y-direction, as shown in Figure 3-1. Table 3-1 lists the detail of the grid, which includes the mesh resolution in wall units. The resolution is calculated as $\triangle_y^+ = \frac{\triangle y u_\tau}{\nu}$. The averaged local friction velocity, u_τ is defined based on the $u_\tau = \sqrt{\frac{\tau_w}{\rho}}$.

Table 3-1 Detail of grid.

ξ × η × ζ	720 × 65 × 33
# nodes along the wake (ξ-direction)	151
# nodes on pressure side (ξ-direction)	211
# nodes on suction side (ξ-direction)	211
Cell sizes at leading edge (height)	$5 \times 10^{-5}C$
Cell sizes at trailing edge (height)	$5 \times 10^{-5}C$
$\Delta x^+, \Delta y^+, \Delta z^+$ (wall units)	90~700, 2~14,100~900
Computational domain	$20C \times 20C \times 0.4C$

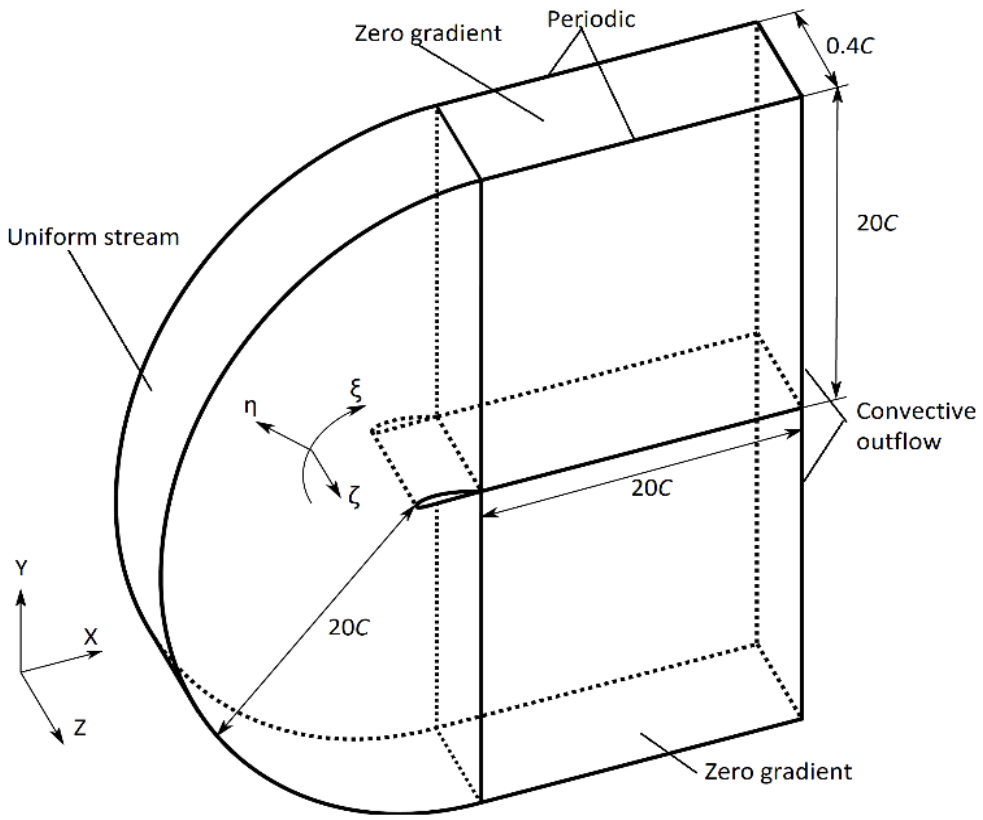

Figure 3-1 Computational domain for C-type grid.

3.2.1 Boundary Conditions

The cylindrical surface of the upstream side of the computational domain was set as an inlet boundary condition where the freestream velocities U_∞ without turbulence was used. At the top and bottom boundaries, the normal components of the gradients of variables were set to zero. Convective boundary conditions $\frac{\partial \bar{u}_i}{\partial t} + U_\infty \frac{\partial \bar{u}_i}{\partial x} = 0$ were applied as outlet boundary conditions. In addition, the no-slip boundary condition was enforced around the airfoil. In the spanwise direction, a periodic boundary condition was employed. For the pressure boundary conditions, a Neumann boundary condition $\frac{\partial \bar{p}}{\partial n} = 0$ was implemented for inflow, outflow, top, and bottom boundaries.

3.3 Results and Discussion

3.3.1 Laminar transition

In this simulation, no ad-hoc method was used as a treatment for the laminar-transition region. The subgrid scale kinetic energy k_{SGS} was set to zero at the wall, and a clipping procedure was

implemented for the negative $k_{SGS.}$ This clipping procedure is required to ensure the eddy viscosity v_t in the equation of motion is always positive. Based on previous experience, the OD model's stability has been proven despite no averaging in a homogeneous direction to calculate the coefficient. The initial data was taken from a fully developed stage of DSM simulation, where at the first step, the k_{SGS} was calculated via equation (2-8). The statistical data was collected for 9.3-time units (C/U_∞).

Figure 3-2 displays the time and spanwise averaged velocity vectors and instantaneous k_{SGS} contour plot. The instantaneous k_{SGS} is plotted as a background to visualize the location of the k_{SGS} development. The velocity vector in Figure 3-2 displays a thin laminar boundary layer developed around the leading edge. On the other hand, the subgrid scale kinetic energy k_{SGS} starts to develop after x/C = 0.11. The ONERA wind tunnel results revealed that the thin laminar boundary layer was also developed around the leading edge, a laminar separation bubble was formed, and the flow reattached around x/C =0.12 [3].

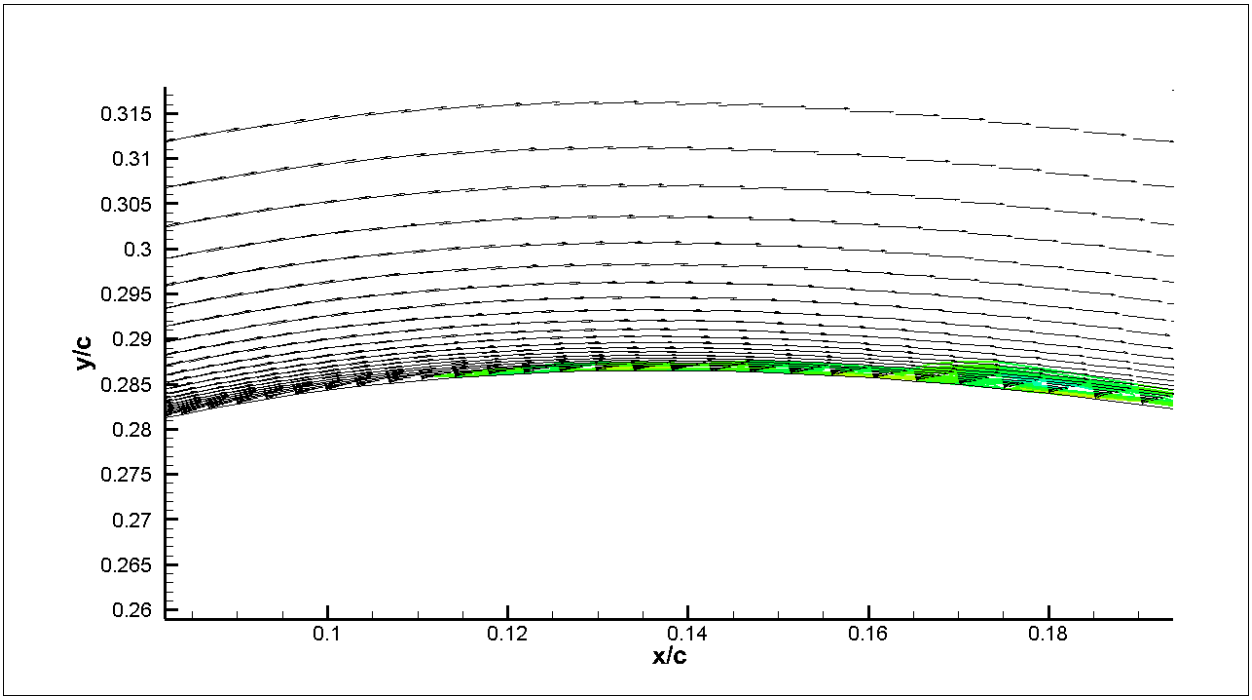

Figure 3-2 Averaged velocity vectors around leading edge at slice z/C = 0.2.

Figure 3-3 shows the normal components of Reynolds stress around the suction side of the airfoil. The figure axis R11 and R22 denote the normal component of Reynolds stress corresponds to the direction parallel and normal to the airfoil wall, respectively. While R33

corresponds to the spanwise component. Two graphs are plotted around $y/C = 0.0003$ and $y/C = 0.001$. The results, that is, without turbulence stress, indicate that the laminar region is successfully captured. The results also show that the OD model reduces the dependency of fine grid resolution to capture a very thin laminar boundary layer.

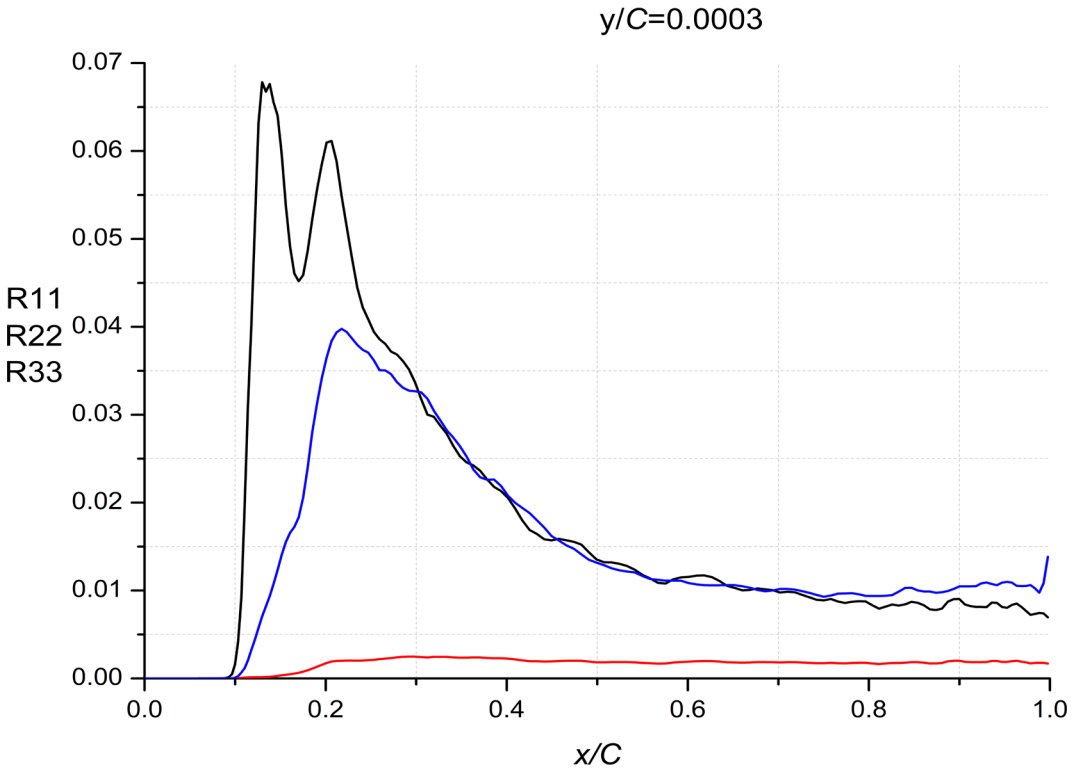

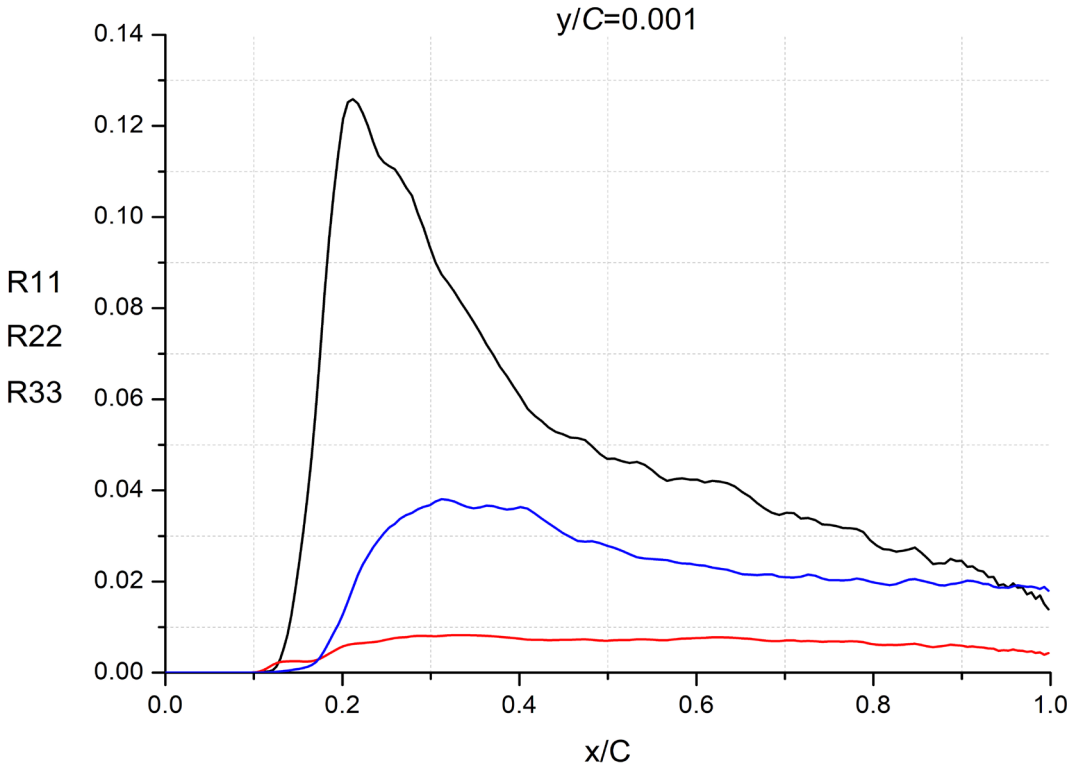

Figure 3-3 Normal components of Reynolds stress at y/C = 0.0003 and y/C = 0.001.(Black, R11 Blue, R22 Red, R33)

3.3.2 Pressure coefficient and skin friction coefficient

The profiles of the mean pressure coefficient $C_P = 2(p - p_\infty)/\rho U_\infty^2$ and skin friction coefficient $C_f = 2\tau_\omega/\rho U_\infty^2$ ($\tau_\omega$represents the wall shear stress) are plotted in Figure 3-4. In the LESFOIL project, the plots of C_p and $C_f$are very important to justify the existence of the laminar separation bubble around the leading edge and the separation around the trailing edge [2], [3], [36]. For the simulation, this phenomenon is commonly described by looking at the plateau of the C_p plot and the negative value of skin friction coefficient C_f. Unfortunately, this phenomenon cannot be captured by the OD model where no plateau is observed around the leading edge, and the C_f plot also displays a positive value around this region.

For the skin-friction coefficient C_f, the wall shear stress is defined as $\tau_\omega = \mu \left(\frac{\partial u_b}{\partial n}\right)_{n=0}$ where u_b is the velocity component along the airfoil surface. The result of the OD model is not identical to the experimental data. Insufficient resolution for streamwise and spanwise direction is found to be one of the reasons for the underprediction of the skin-friction coefficient. To date, previous results from LESFOIL documents have revealed that the resolution $\triangle_x^+ = 60 - 100$, $\triangle_y^+ = 2$ $\triangle_z^+ = 25 - 40$ [1], [4], [37] is required to match the C_f with experimental data. A

recent update from Asada and Kawai [2] has revealed that $\triangle_x^+ = 25$, $\triangle_y^+ = 0.8$ $\triangle_z^+ = 13$ agrees well with the experimental data. In this simulation, the resolution does not reach the required mesh resolution and as a consequence, the development of turbulent structures is not accurately represented [1]. In addition, the one-equation SGS model alone is insufficient to represent an accurate result for the skin friction. For the current simulation, the fine mesh resolution was found to outweigh the effect of the SGS models.

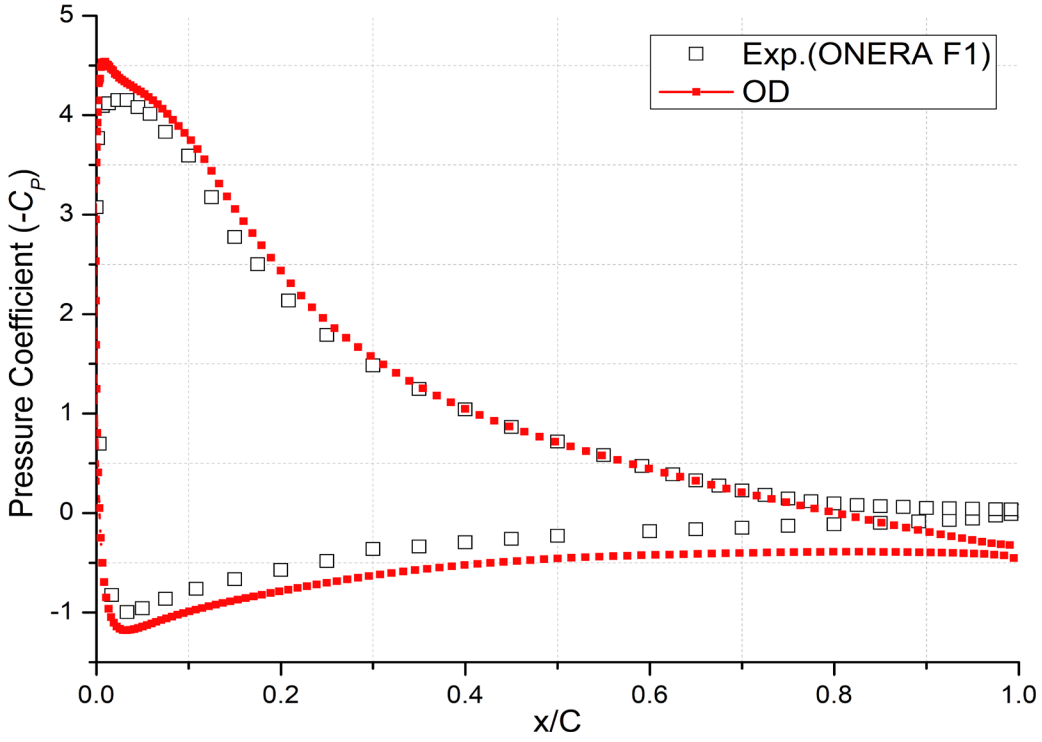

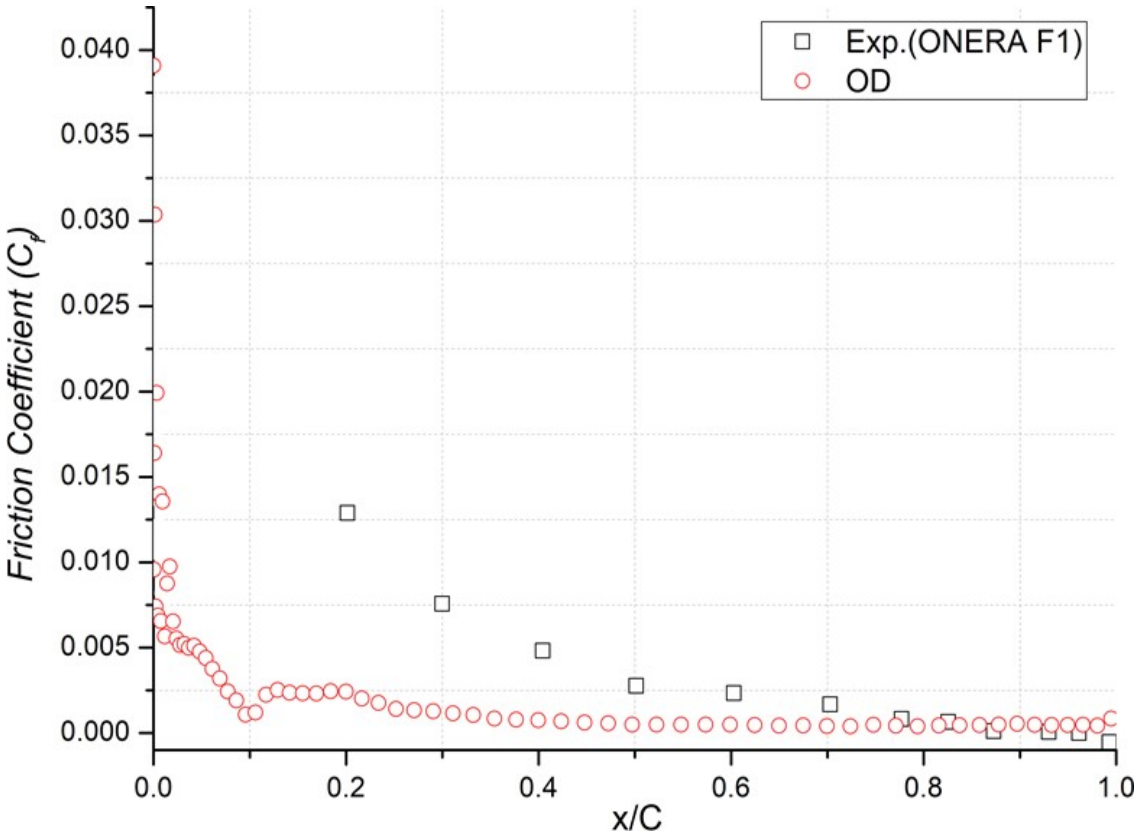

Figure 3-4 Averaged pressure coefficient C_p and friction coefficient C_f.

3.3.3 Total Turbulent Kinetic Energy

Total turbulent kinetic energy is defined as a summation of subgrid scale turbulent kinetic energy k_{SGS} and grid scale turbulent kinetic energy, $k_{GS} = \frac{u'^2+v'^2+w'^2}{2}$. In the OD model, the production term $-\tau_{ij}\bar{D}_{ij}$ is described differently from other dynamic versions of the one-equation model. Figure 3-5 shows the k_t and k_{SGS} plotted at the location of y/C =0.0003 and y/C = 0.001. From these plots, the dynamic procedure implemented in the production term manages to identify the non-turbulent region around the leading edge, in contrast to the conventional eddy viscosity model where SGS eddy viscosity v_t exists due to the velocity gradient even in the laminar region. Furthermore, at y/C = 0.0003, the first peaks for k_t and k_{SGS} are identical to each other at approximately x/C = 0.13. These peaks are possibly associated with the location of flow reattachment phenomena. These peaks are also identical to the normal component of Reynolds stress (Figure 3-3), where the flow from the laminar region (no resolved stresses) reaches the peak as the flow reattaches. This also indicates the beginning of the development of

the turbulent boundary layer. A similar trend is observed for both locations except for the peak of kinetic energy. Therefore, the OD model resolved the issue of removing the turbulent kinetic energy and eddy viscosity in the laminar region without any artificial methods and grid refinement.

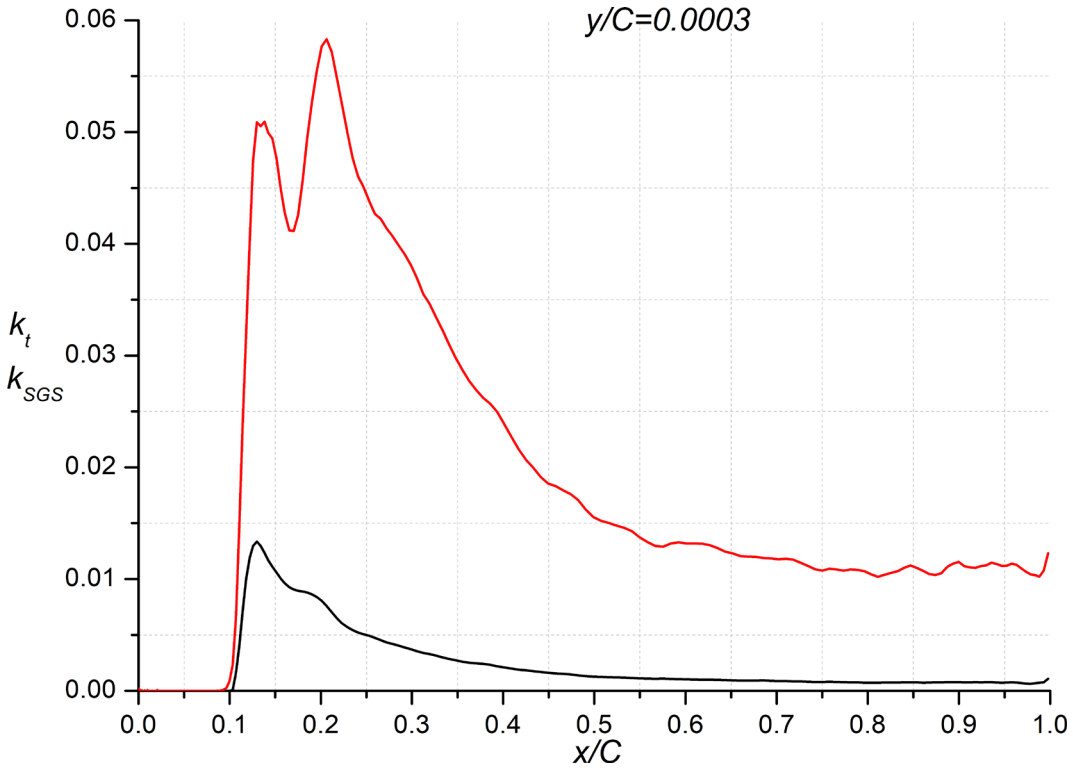

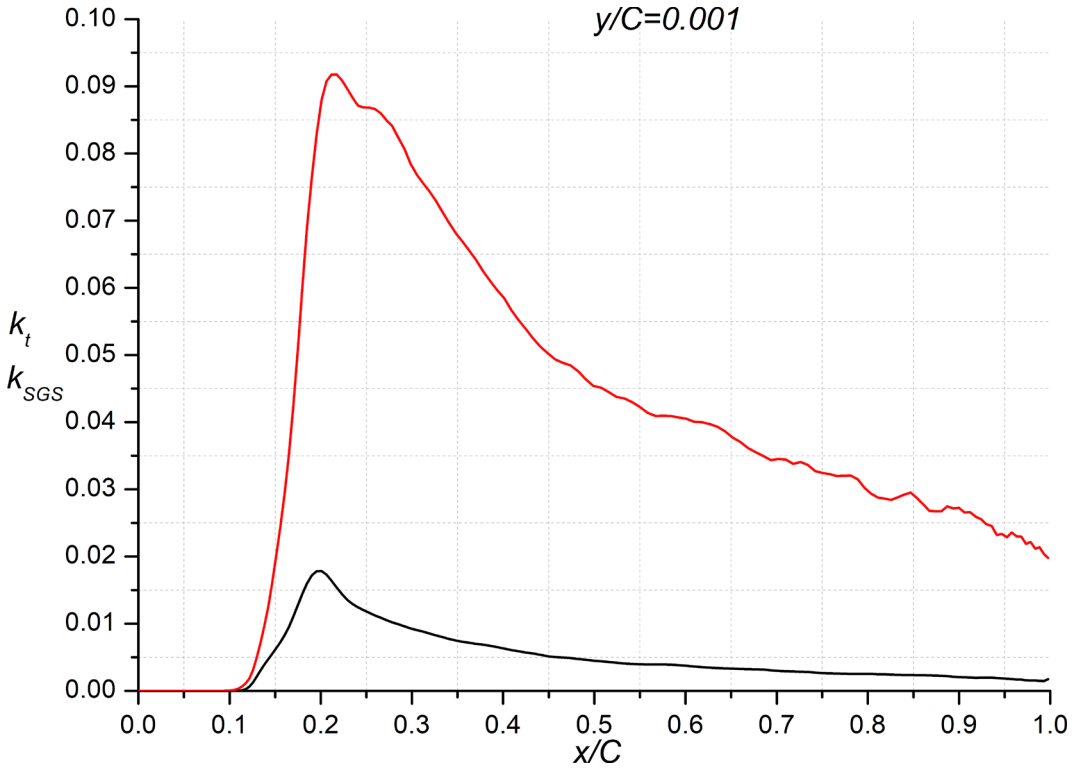

Figure 3-5 Averaged total turbulent kinetic energy (k_t)-red line and SGS kinetic energy (k_{SGS})-black line around suction side of the airfoil.

The dynamic procedure implemented for the OD model revealed that the total kinetic energy remained zero in the laminar region and switched to some finite value in the transition to the turbulent region. In the OD model, the dynamic procedure was applied to determine the coefficient in the production term of turbulent kinetic energy equation k_{SGS}. As described in section 2.3, the dynamic procedure to evaluate the coefficient in production term could become negative, and as a consequence, would lead to a decrease in k_{SGS}. The advantage of applying the eddy viscosity model of Smagorinsky type in production term was proven in this study where there was no self-reproduction of k_{SGS} in the laminar region as highlighted by Inagaki and Abe [32] and Davidson [33]. The clipping of k_{SGS} also led other terms in the transport equation of k_{SGS} to become zero in the laminar region. On the other hand, the terms in k_{SGS} transport equation should be balance in the turbulent region, especially in the vicinity of the wall.

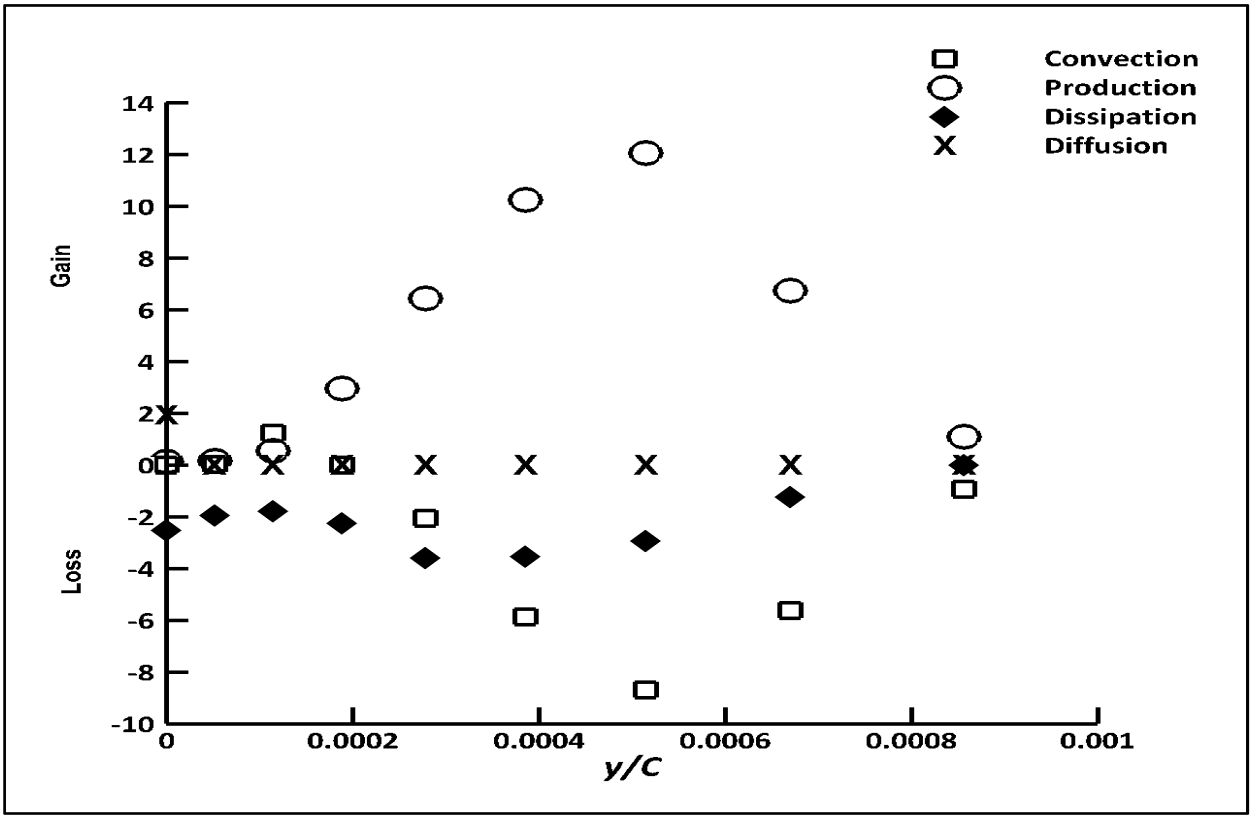

Figure 3-6 Budget of SGS kinetic energy at x/C = 0.12.

In order to ensure the balance of terms in k_{SGS} equation, the averaged of production, convection, diffusion, and dissipation terms in the transport equations of k_{SGS} or the budget of SGS kinetic energy were plotted in Figure 3-6. This figure is plotted at the location of x/C = 0.12, which indicates the laminar-transition region. It is evident that the terms in the energy budget are relatively important in the vicinity of the wall. The transport equation for k_{SGS} based on the OD model reveals that the production term is balanced with the summation of dissipation and convection terms. On the other hand, the diffusion and dissipation from molecular viscosity and additional dissipation terms (see Eq. 2-17) are almost balanced on the wall. In the OD model, the dissipation term is defined as a summation of the SGS dissipation term and the additional dissipation term (terms 2 and 3 in Eq. 2-16). Hence, the additional dissipation term of Eq. 2-17 is important for the OD model in the vicinity of the wall.

3.4 Concluding Remarks

This chapter deals with the application of the OD model for flows over A-profile airfoil near to the stall condition. The OD model was used to predict the laminar-transition region, where the

coefficient in the production term was calculated dynamically. In contrast to what is commonly used to predict the laminar-transition region, the OD model revealed that no unique procedure was required to vanish the eddy viscosity in the laminar region. This chapter also presents several contributions. Firstly, the plots of k_{SGS} revealed that no SGS kinetic energy was reproduced in the laminar region. The finite value of k_{SGS} indicated the reattachment point, and this point was observed in agreement with the experimental data. Secondly, the plots of Reynolds stress also discovered that no turbulent stress was observed in the laminar region. Thirdly, the balance of terms in k_{SGS} was confirmed. Findings from this chapter revealed that the OD model was able to predict the laminar-transition region without any special treatment.

CHAPTER 4

Dynamic Stall Simulation of Oscillating NACA0012 Airfoil

4.1 Governing Equation

In this calculation for unsteady pitching airfoil, the filtered Navier-Stokes equations are defined here in a non-inertial frame of reference

$$\frac{\partial \bar{u}_i}{\partial x'_i} = 0 \tag{4-1}$$

$$\frac{\partial \bar{u}_i}{\partial t} + \frac{\partial (\bar{u}_i + 2\epsilon_{imn}\Omega'_m x'_n)\bar{u}_j}{\partial x'_j} = -\frac{\partial}{\partial x'_i}(\bar{P}) + \nu \frac{\partial^2 \bar{u}_i}{\partial x'_j x'_j} - \frac{\partial \tau_{ij}}{\partial x'_j} - \epsilon_{ijk}\frac{\partial \Omega'_j}{\partial t} x'_k - \epsilon_{ijk}\epsilon_{mnk}\Omega'_j \Omega'_m x'_n \tag{4-2}$$

where $\bar{P}$ is the effective pressure, ν is the kinematic viscosity, ϵ_{ijk} is Levi-Civita's alternating tensor, $\bar{u}_i$ is the filtered velocity, and the Ω'_i is defined as the angular velocity component of the non-inertial system. For the coordinate system, x'_i is derived based on the transformation in a non-inertial frame of reference. For this simulation, the axis of rotation is in x_3 direction. The effect of system rotation appears as the Coriolis term, centrifugal term, and angular acceleration component of the non-inertial system resulted from coordinate transformation for time derivative term and nonlinear convective term. The detail of the derivation can be found in Appendix A.

Equations 4-1 and 4-2 are transformed into a general curvilinear coordinate system, as shown below

$$\frac{1}{J}\frac{\partial (J\bar{U}^k)}{\partial \xi'^k} = 0, \tag{4-3}$$

$$\frac{\partial \bar{u}_i}{\partial t}+\frac{1}{J}\frac{\partial J(\bar{u}_i+2\epsilon_{imn}\Omega'_m x'_n)\bar{U}^k}{\partial \xi'^k} \qquad 4\text{-}4$$
$$=-\frac{1}{J}\frac{\partial \xi'^k}{\partial x'_i}\left(J\frac{\partial(\bar{P})}{\partial \xi'^k}\right)+\nu\frac{1}{J}\frac{\partial}{\partial \xi'^k}\left(\gamma^{jk}\frac{\partial \bar{u}_i}{\partial \xi'^k}\right)-\frac{1}{J}\frac{\partial}{\partial \xi'^k}\left(J\frac{\partial \xi'^k}{\partial x'_j}\tau_{ij}\right)$$
$$-\epsilon_{ijk}\frac{\partial \Omega'_j}{\partial t}x'_k-\epsilon_{ijk}\epsilon_{mnk}\Omega'_j\Omega'_m x'_n$$

In order to solve SGS stress, similar procedures explained in Chapter 2 are also executed here. In addition, all the coordinate systems are derived based on the transformation in the non-inertial frame of reference. The transport equation for SGS kinetic energy, k_{sgs} is defined as

$$\frac{\partial k_{sgs}}{\partial t}+\frac{\partial}{\partial x'_j}\left(\bar{u}_j k_{sgs}\right)=P_{k_{sgs}}-C_\varepsilon\frac{k_{sgs}^{\frac{3}{2}}}{\bar{\Delta}}-\varepsilon_\omega+\frac{\partial}{\partial x'_j}\left[\left(\nu+C_d\Delta_v\sqrt{k_{sgs}}\right)\frac{\partial k_{sgs}}{\partial x'_j}\right]. \qquad 4\text{-}5$$

This transport equation is also presented in a non-inertial frame of reference. In most studies, the SGS models such as Smagorinsky model (SM), dynamic Smagorinsky model (DSM), and One-equation SGS kinetic energy are fundamentally based on the assumption that the small scale turbulence is nearly homogeneous and isotropic, hence the rotation effects (Coriolis and Centrifugal) are not counted in the equation [38]. Tsubokura et al. [39] conducted a study to evaluate the effect of a rotating term such as Coriolis force in the SGS model; they have concluded that the velocity profiles, grid scale (GS) Reynolds stress, and GS turbulent intensities are independent of the rotating effect. Squires and Piomelli [40] found that the DSM without any modification to account for rotation has performed well in the rotating channel flow where good agreement with experimental data and DNS is observed for mean velocities and turbulent intensities.

To date, most simulations based on the one-equation model have been performed without explicitly accounted for any rotating terms (Coriolis force). The difficulty in deriving that equation in the rotating frame is one of the reasons where the directional and two-point information are required [40]. Therefore, various additional ad-hoc modifications were proposed to account for the rotating flows. In addition, as far as LES is concerned, the impact of system rotation on SGS is less dominant than the local rotation rate of the GS [34], [39]; therefore, the author did not make any modifications to the model.

4.2 Computational Setup

This study focuses on the dynamic stall simulation around NACA0012 at a Reynolds number of 1.35×10^5 based on chord length and freestream velocity. This range of Reynolds number is believed to provide a well-resolved large-eddy simulation and is within the range of the developed turbulent boundary layer before the dynamic stall takes place [11], [16]. This setup corresponded to the wind tunnel experiment setup conducted by Lee and Gerontakos [10]. Their experiment was conducted based on a 0.15 *m* chord length (c) and 2.5c span. The freestream velocity was 14 *m/s,* and the turbulence intensity of 0.08% was measured at freestream velocity.

In this study, the airfoil performs the pitching motion based on the sinusoidal mode where

$$\alpha(t) = \alpha_{mean} + \alpha_{amp}\sin\left(\frac{2kU_\infty}{c}t\right). \qquad 4\text{-}6$$

The α_{mean} and α_{amp} represent the mean angle of attack and amplitude, respectively. The pitching axis is located at the quarter chord from the leading edge. The $k = \pi fc/U_\infty$ is reduced frequency. The α_{mean} and α_{amp} were set to 10° and 15°, respectively. These prescribed kinematic parameters would result in $\alpha_{min} = -5°$ and $\alpha_{max} = 25°$, where the importance of dynamic stall phenomena such as leading-edge vortex (LEV), shedding of LEV, trailing-edge vortex (TEV), and the interaction with boundary layer could be evaluated. For the same kinematic parameters, previous researchers varied the reduced frequency, k [23], [24], [41], [42], the effect of unsteady freestream velocity [24], grid resolution, and domain size effect [24]. A summary of a recent publication on the oscillating airfoil is listed in Table 4-1.

Table 4-1 A review of published study cases on NACA0012.

Authors (year) Reynolds number	Pitching motion	Reduced frequency, k	CFD methods, Turbulence model & dimension	Research area
X. Li et al. (2018) Re_c=2.53×10^5		0.01 – 0.4	uRANS 2D (k-ω & k-ε)	Influence of k, α_{mean}, α_{amp}
Geng et al. (2018) Re_c=1.35×10^5	10°+ 15°sin(ωt)	0.025, 0.05, 0.1	uRANS 2D (SST, SST k-ω) LES 2.5D (Smagorinsky Model Cs =0.1)	Blockage ratio, grid resolution, y+, time step, freestream turbulence at inlet, trailing edge, turbulence model
Visbal & Benton (2018) Re_c=5.0×10^5	4°+7°(1-cos(2kt)	0.2	ILES (high order low -pass filter)	High frequency control (St), LSB
Kim & Xie (2016) Re_c=1.35×10^5	10° + 15°sin(ωt)	0.025, 0.05, 0.1	LES 3D (MTS)	Influence of freestream turbulence on dynamic stall
Gharali & Johnson (2013) Re_c=1.35×10^5	10° + 15°sin(ωt)	0.1	URANS 2D (SST k-ω & k-ε)	Influence of unsteady freestream velocity

4.2.1 Computational Domain and Grid

A typical C-type grid was used in this study where ξ coordinate went around the airfoil and η was in the outward direction from the solid wall and cut-line after the trailing edge. Meanwhile, ζ was in the spanwise direction. The domain was extended 0.1c in a spanwise direction and had a uniform spacing. A study by Visbal and Garmann [12] showed that the spanwise extension of 0.1c was sufficient to capture the LEV and dynamic stall vortex (DSV). The domain size for the X and Y direction was extended to 20c, as shown in Figure 4-1. This domain extension was found sufficient to hinder the boundary reflections [23].

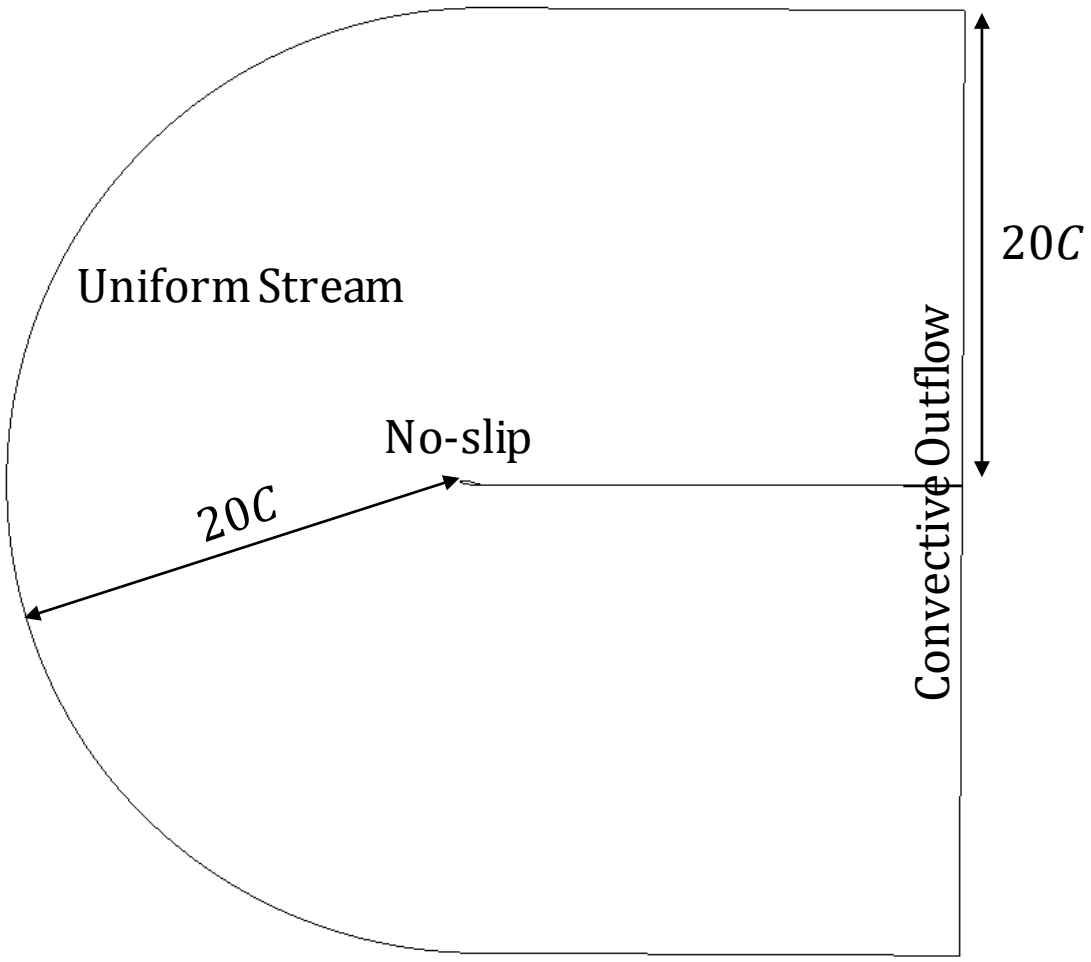

Figure 4-1 Computational Domain and boundary conditions.

The grid was designed to have more concentrated nodes near the airfoil to ensure the $y^+ \leq 1$ in order to capture the boundary layer separation and reattachment. Hence, the heights of the first node adjacent to the airfoil wall were set to 1×10^{-4} and 3×10^{-4} around the leading and trailing edge, respectively. The finished *C*-mesh around the airfoil, leading, and trailing edge are shown in Figure 4-2. The details of the grid parameter are listed in Table 4-2.

Table 4-2 Grid Parameters.

Grid Type	*C*-grid
# of points along the wake	65
# of points on the pressure side	193
# of points on the suction side	386
# of points on wall normal	50
# of points spanwise	33, 66
L_z/c	0.1

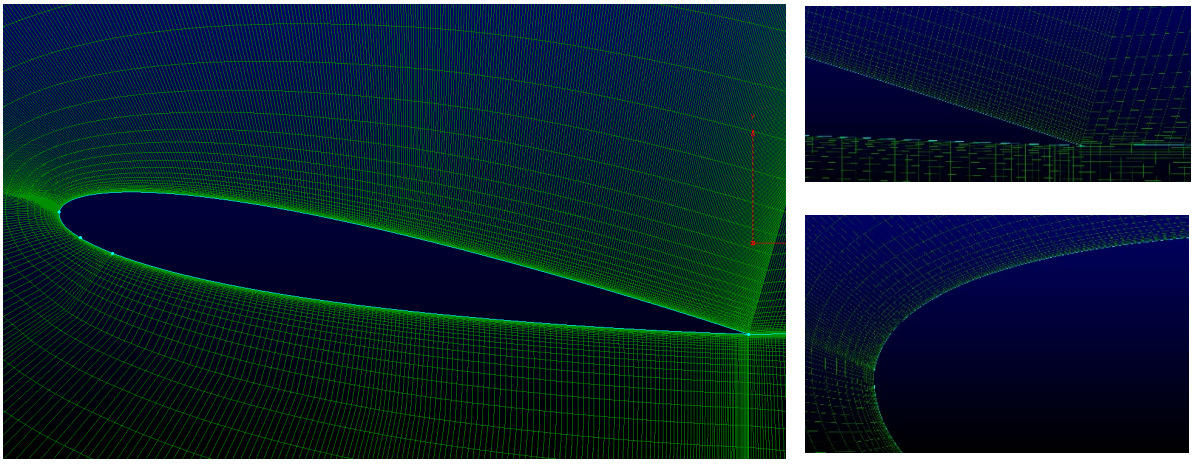

Figure 4-2 C-type mesh around NACA0012 (trailing edge and leading edge).

4.2.2 Boundary Conditions

The no-slip boundary condition was imposed at the solid wall around the airfoil. The convective outlet boundary condition was used at the velocity outlet. For the inlet, freestream velocity without disturbance was set around the *c*-curve. The periodic boundary condition was applied to the spanwise direction. The computational domain and the respective boundary conditions are shown in Figure 4-1.

4.2.3 Numerical Procedure

The spatially filtered Navier-Stokes Equations (NSE) were solved using in-house finite difference method code. The influence of the rotational effect was added in the momentum equation, as shown in Eq. 4-2. The nonlinear term was discretized based on the quadratic

upstream interpolation for convective kinematics (QUICK) upwinding scheme. In our calculation, the kinetic energy of the SGS transport equation also needed to be solved. For the nonlinear term, the donor cell method was adopted. For the diffusion term, the 2nd order central finite difference method was applied. In order to solve the temporal discretization, an explicit time stepping procedure based on the Adams-Bashforth method of the 2nd order accuracy was used. For this calculation, the non-dimensional time step was set to $\frac{\Delta t U_\infty}{c} = 3 \times 10^{-5}$ to provide enough temporal resolution of SGS features. The Poisson equation was solved with the SOR (successive over-relaxation) method.

4.3 Results and Discussion

4.3.1 Numerical Configuration

The results discussed in this section are associated with two and three-dimensional simulations. A similar grid was used for both simulations. For the 3-dimensional grid arrangement, the number of grid points in the spanwise direction was set to 33 and 66. For the 2-dimensional simulation, the number of grid points in the spanwise direction was only set to 2 points, with spanwise extent *z/C* was set to 0.002. The information about the *C*-grid arrangement is listed in Table 4-2.

4.3.2 Three-Dimensional (3-D) Simulations

For all computations, the reduced frequency, $k = \pi f c / U_\infty = 0.3$ was set. In order to resolve adequate temporal resolution of the fine scale structures, a very small non-dimensional time step was initiated. As a result of these parameters, the non-dimensional period of the motion was $T = 10.5$. On top of that, 350,000-time steps were required to complete one pitching cycle. Due to the limitations in computational time, the 3D simulations were run for only 1.5 cycles. This is a common practice for 3D LES simulations for the oscillating airfoil, where only 1 or 2 cycles are simulated [15], [43].

In order to investigate the effects of grid resolution in the spanwise direction, two different grid numbers were simulated in this study. Figure 4-3 shows a variation of lift and drag coefficient as a function of non-dimensional flow time (t/T) for N_Z=33 and N_Z=66. Note that symbols '↑' and '↓' refer to upstroke and downstroke motions, respectively. Generally, the drag and lift coefficients increase during upstroke motion and reach the peak value at the maximum

pitching angle. However, this trend is not identical for the drag coefficient, where the peak value is observed beyond the maximum angle of attack (around $\alpha = 24° \downarrow$). After reaching the peak value, both drag and lift coefficients exhibit a sudden drop, which represents the dynamic stall. For the simulated operating conditions, a large difference peak value for coefficients between cycle-to-cycle at a high angle of attack during upstroke and downstroke motion is clearly observed. This phenomenon is expected due to the dynamic stall phenomena such as large separation at trailing edge, effects of transition movement, and turbulence [44], [45].

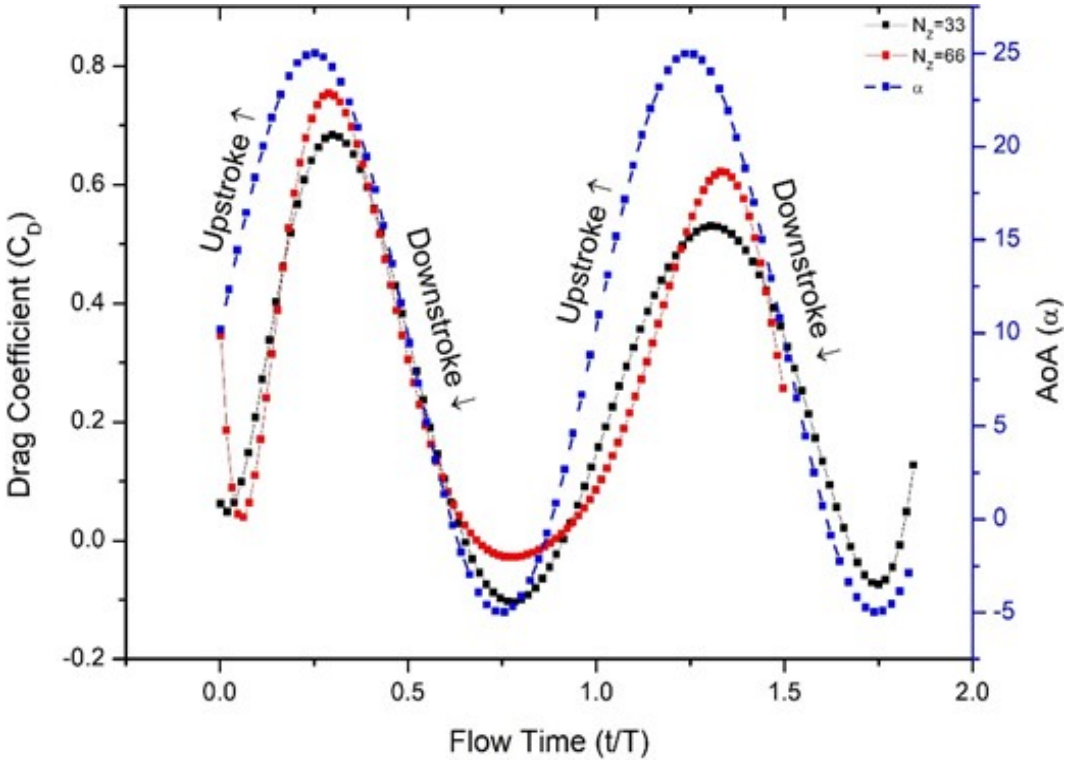

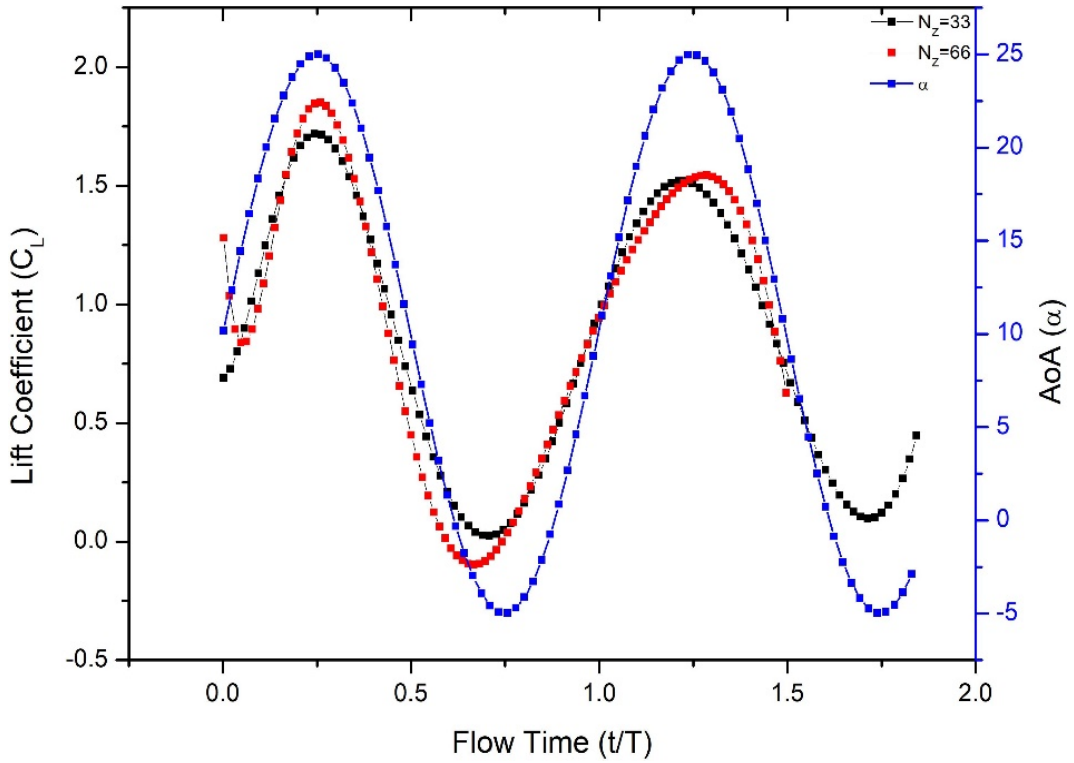

Figure 4-3 Coefficient of drag (C_D) and lift (C_L) versus non-dimensional flow time (t/T). The Angle-of-attack (AoA) is on the right axis.

Figure 4-4 shows the time and spanwise averaged pressure coefficients (C_P) for selected upstroke and downstroke pitching motions. The first LEV is detected at 20°↑. The size of the LEV increases as the angle of attack increases. This event leads to the vortex shedding mechanism. At the maximum angle of attack 25°↑, the LEV is convected on nearly half of the airfoil's suction side; at the same time, the DSV also appears, as shown Figure 4-5. Consequently, the airfoil lift drops.

In the region of the downstroke phase, the vortex is shedding downstream. At 17°↓, the counter-rotating vortex appears at the trailing edge. This counter-rotating vortex also increases in size as the angle of attack decreases. This can be seen in the pressure distribution, where the suction pressure peaks at the trailing edge. Finally, this vortex merges with the first LEV and convects into the wake. At this angle of attack, the lift and drag continue to decrease.

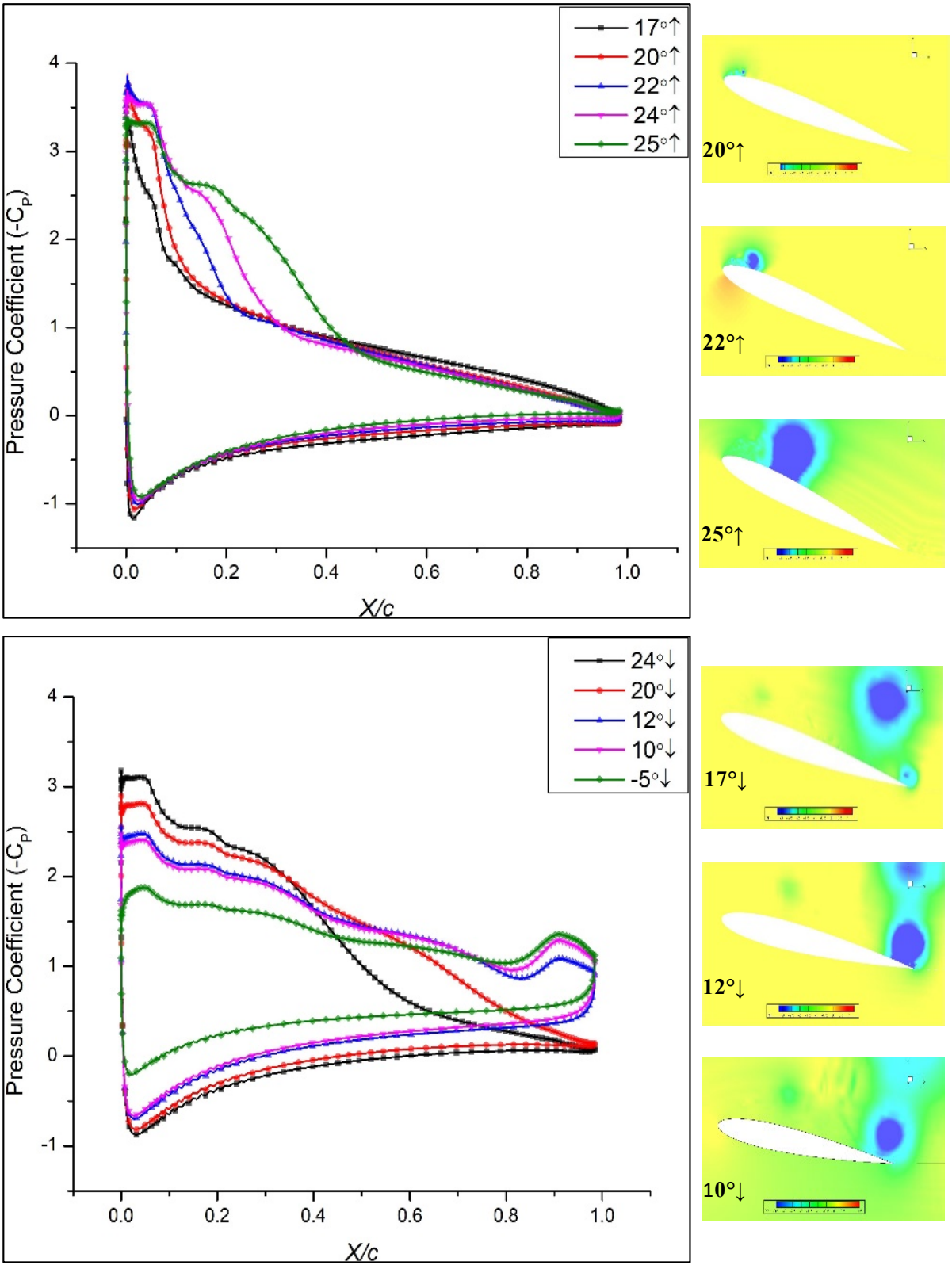

Figure 4-4 Time and spanwise averaged pressure coefficient (C_p)

The Q-criterion [46] is used to observe vortical phenomena in dynamic stall simulations. The Q-criterion is defined as the second invariant of the GS velocity gradient tensor. The unsteady flow field for the upstroke and downstroke phases based on Q-criterion colored by streamwise velocity are shown in Figure 4-5. From 15°↑, development of transitional flow field is observed (marked as 'a'). At 18°↑, a fine-scale structure resulting from spanwise coherent structures from the transition region is formed. This observation was also discussed in detail in the work of [17]. The formation of the LEV is as shown at 20°↑. At the maximum angle of attack (25.0°↑), the LEV becomes larger and convects downstream. At this angle, the airfoil no longer produces lift. In addition, the formation of DSV begins from the downstroke phase until the flow is fully reattached at the beginning of the upstroke phase. The development of DSV is shown in Figure 4-5 for 23°↓, 17°↓ , and 15°↓.

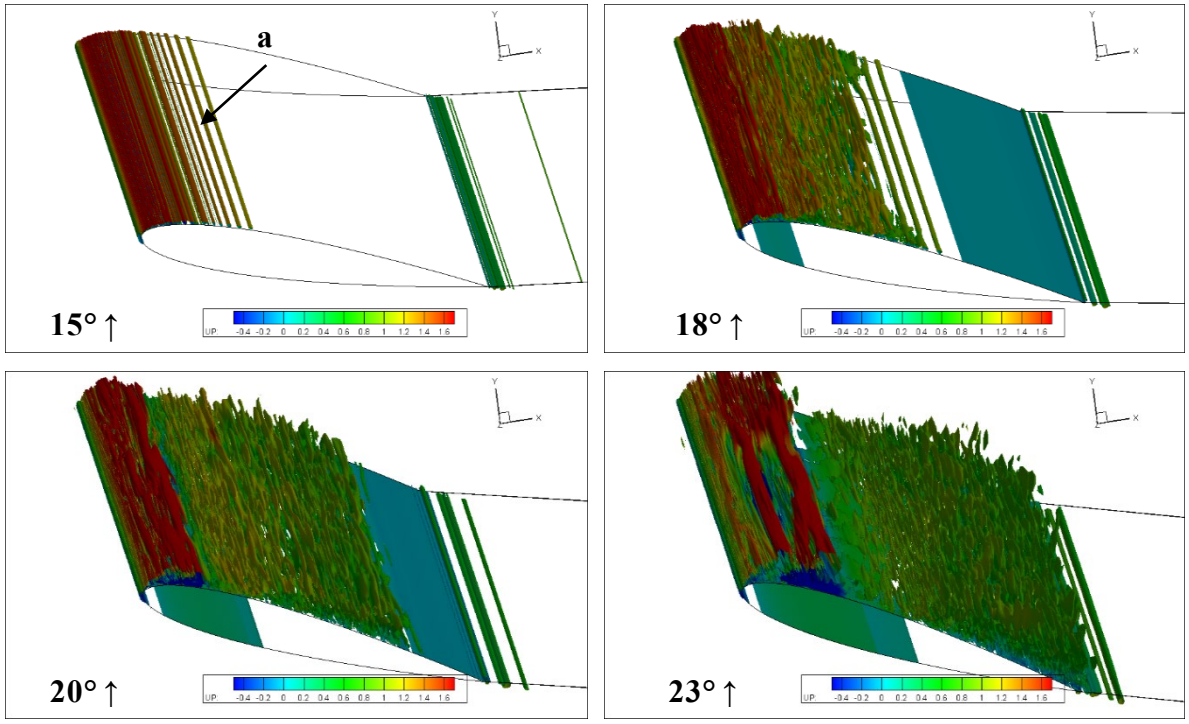

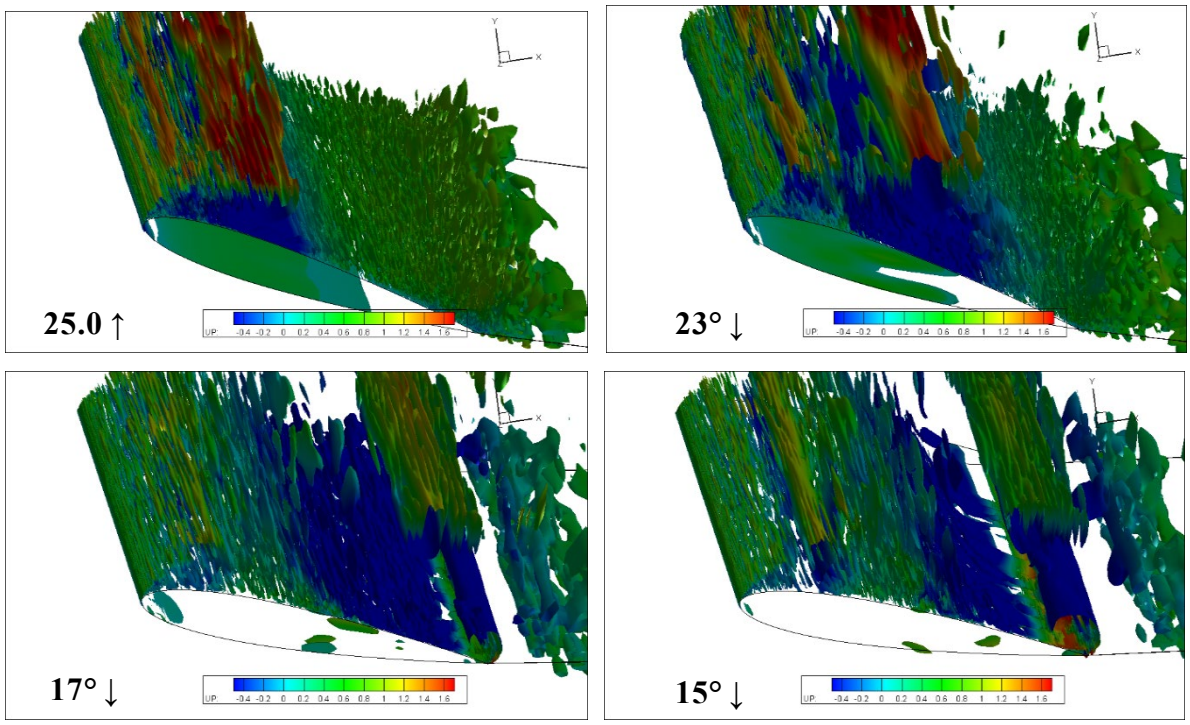

Figure 4-5 Iso-surfaces of Q-criterion colored by streamwise velocity for selected angles (Grid N_z=33).

For deep dynamic stall pitching airfoil, the most complicated flow development was observed during the downstroke phase [10], [23]. Figure 4-6 presents a chronology of vortex development around the suction side of the airfoil. The first vortex is observed around 20°↑. Large separation around the whole suction side of the airfoil is observed at the maximum angle of attack 25°↑. This separation is developed because of strong circulation from the LEV. When the airfoil moves downstroke, the first low-pressure LEV is detached from the airfoil surface and subsequently convected into the wake region. The first LEV in this study grows for about 45% of the chord length compared to the 90% of chord length for the experimental result [10]. This phenomenon leads to the underpredicted of the lift coefficient. The DSV is sweeping around the suction side of the airfoil bringing the low-pressure vortex, and a few vortices around the leading edge are also captured during the downstroke phase. In this study, the development of the TEV is detected at around 17°↓, which deviated from the previous finding where the TEV was detected at 25°↑ [23]. The airfoil regains its aerodynamic forces when the flow is fully attached to the surface, as can be seen at -5°↓.

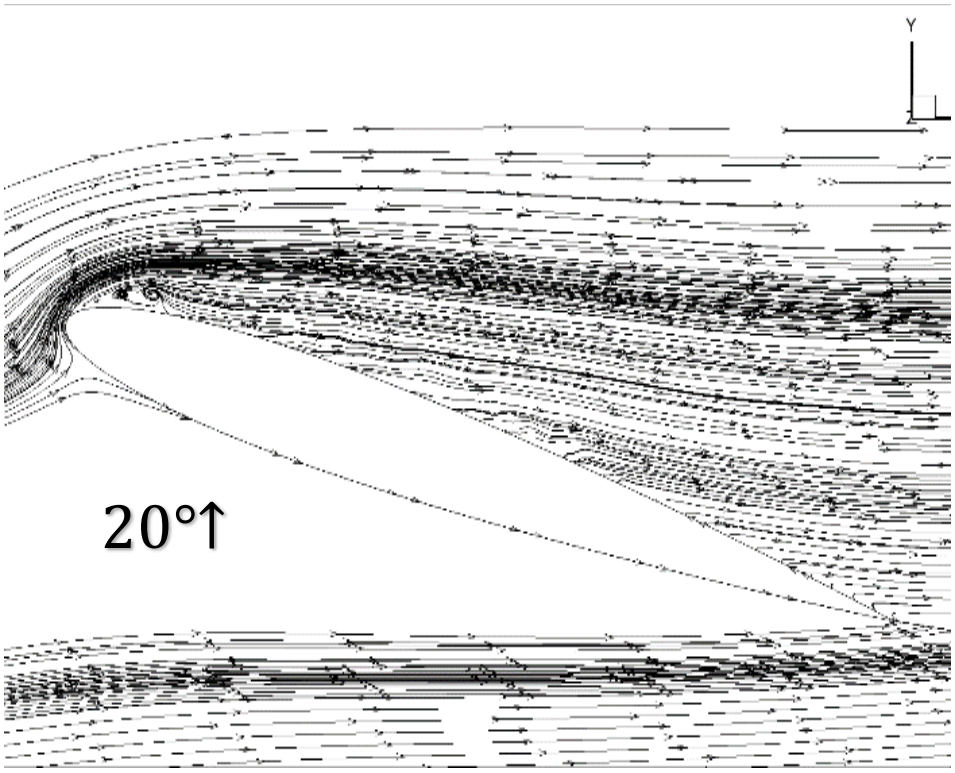
Y
20°↑

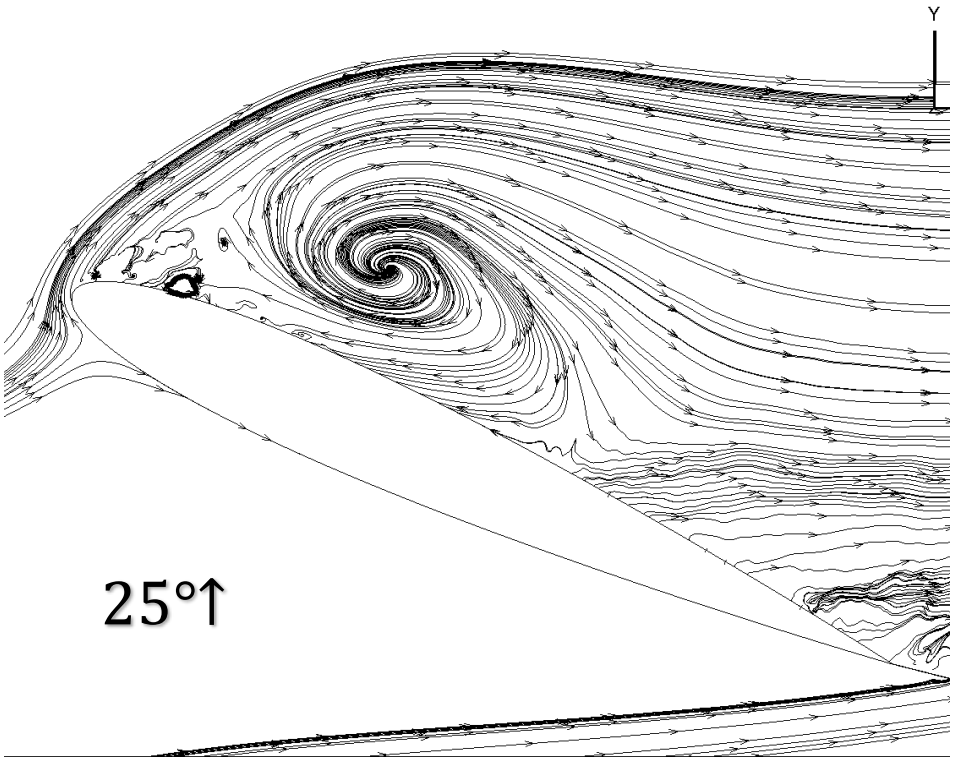
Y
25°↑

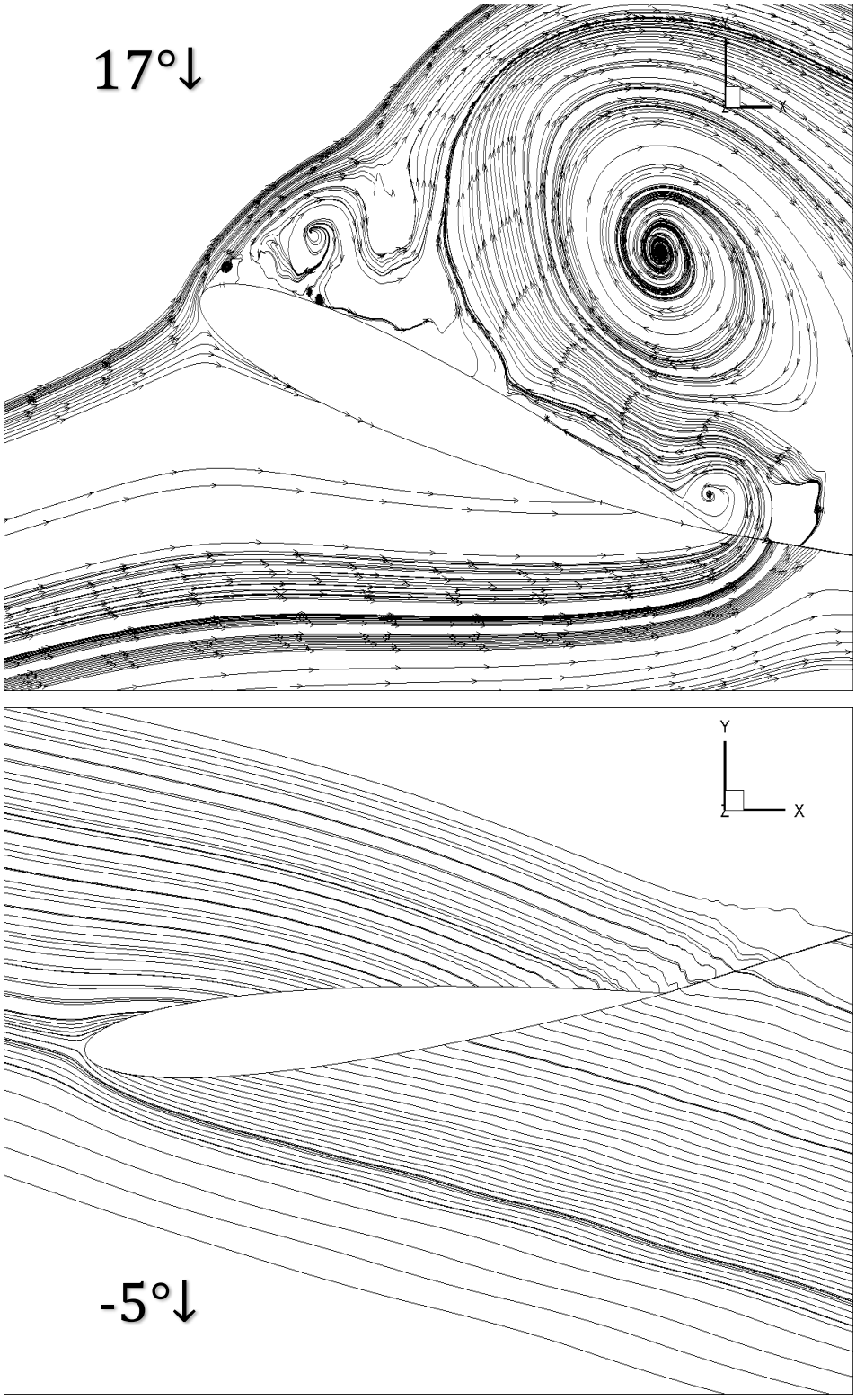

Figure 4-6 Instantaneous Streamlines for selected upstroke and downstroke motion.

Another interesting phenomenon for the deep dynamic stall around unsteady pitching airfoil is the development of a laminar separation bubble (LSB). This phenomenon is unique since the separation occurs in the laminar region. A strong adverse pressure gradient near the leading edge causes the flow separation in the laminar region. The separation in the laminar region is known as the laminar separation bubble (LSB), and the pressure plateau in pressure coefficient plots indicates the size of bubbles. Figure 4-7 exhibits the initiation of the LSB detected at 15.3°↑. A similar finding was observed by Wang et al. [23], where they used the four equations turbulence model (SST-k-ω) to capture the separation bubbles.

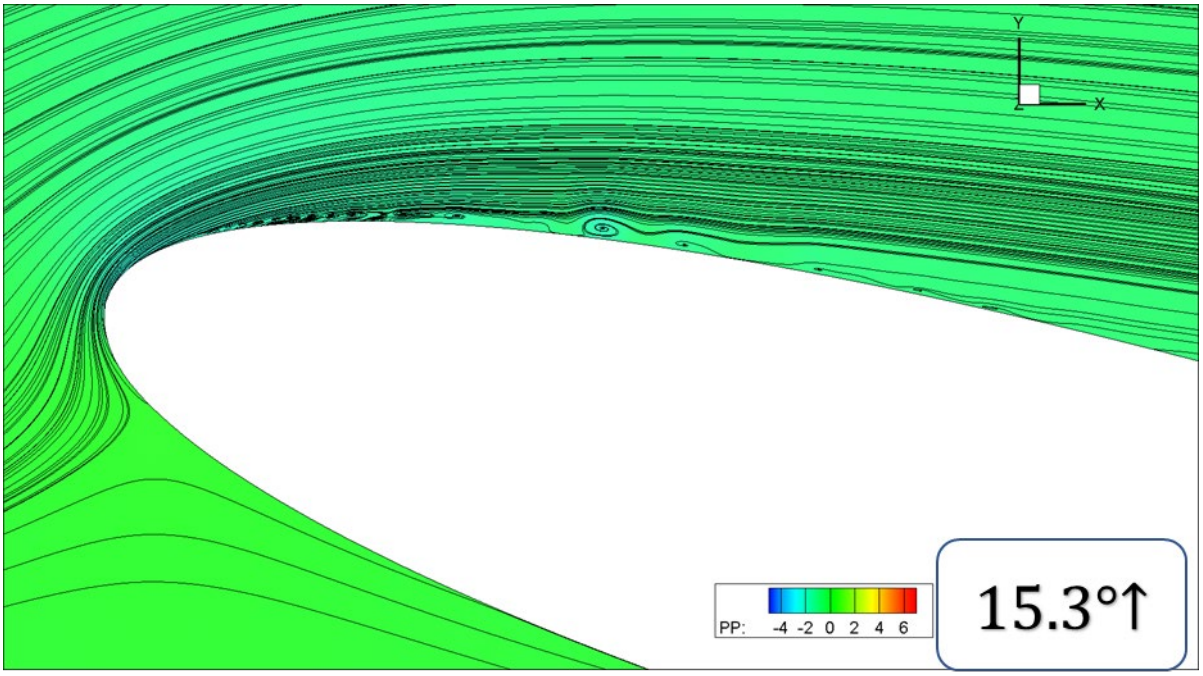

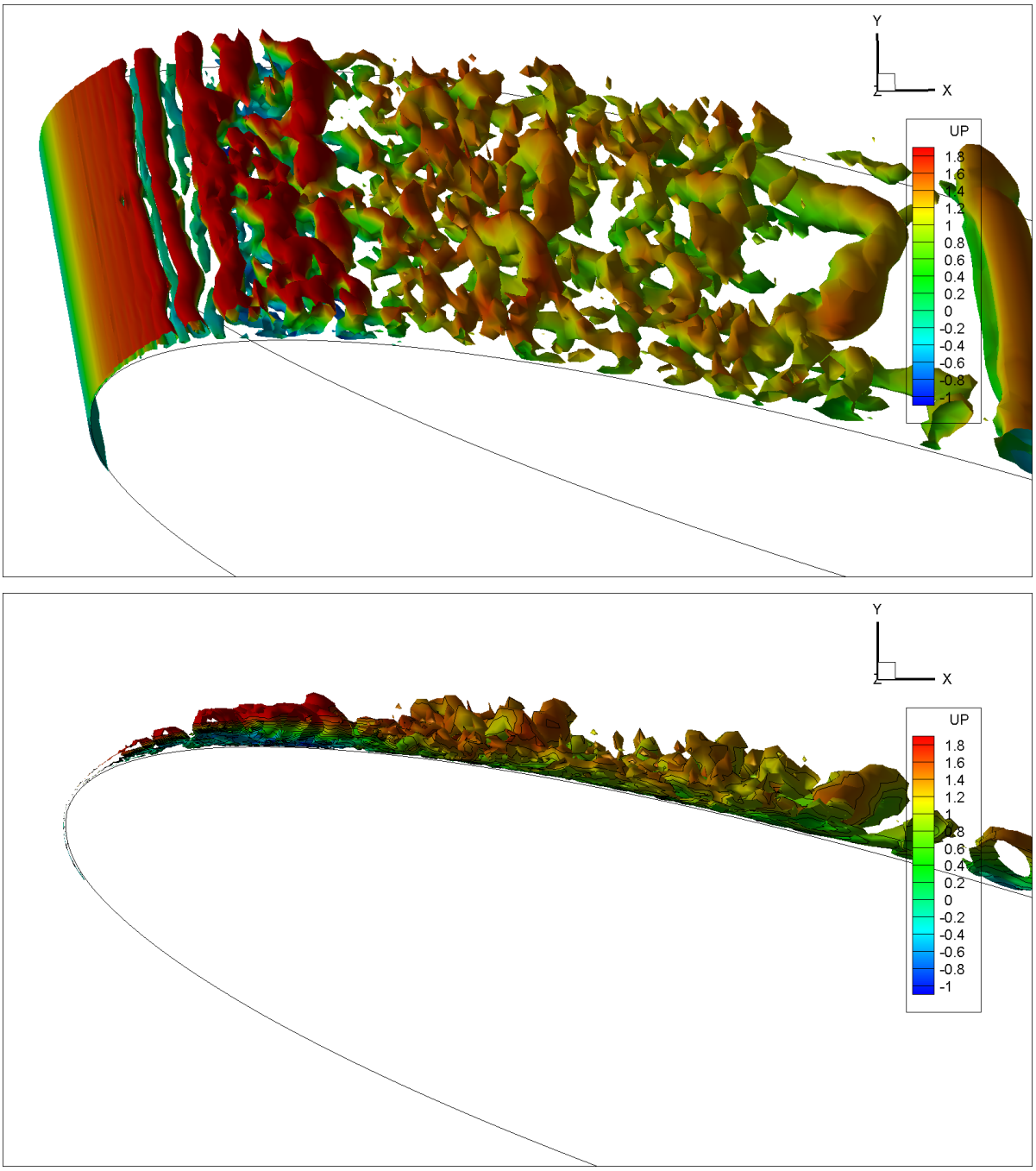

Figure 4-7 Iso-surfaces of pressure colored by streamwise velocity.

Overall, the phenomena which occur around the pitching airfoil are also observed for N_z=66. Figure 4-8 shows the iso-surfaces of Q-criterion based on streamwise velocity for some selected angles of the pitching motion. The hairpin-like vortices are captured during both upstroke and downstroke motions. As a result of vortices breaking down, finer and random well-developed turbulent structures [36] were observed downstream of the airfoil suction side. Additionally,

Kobayashi et al. [47] elaborated that hairpin vortices were related to the forward and backward scatter events.

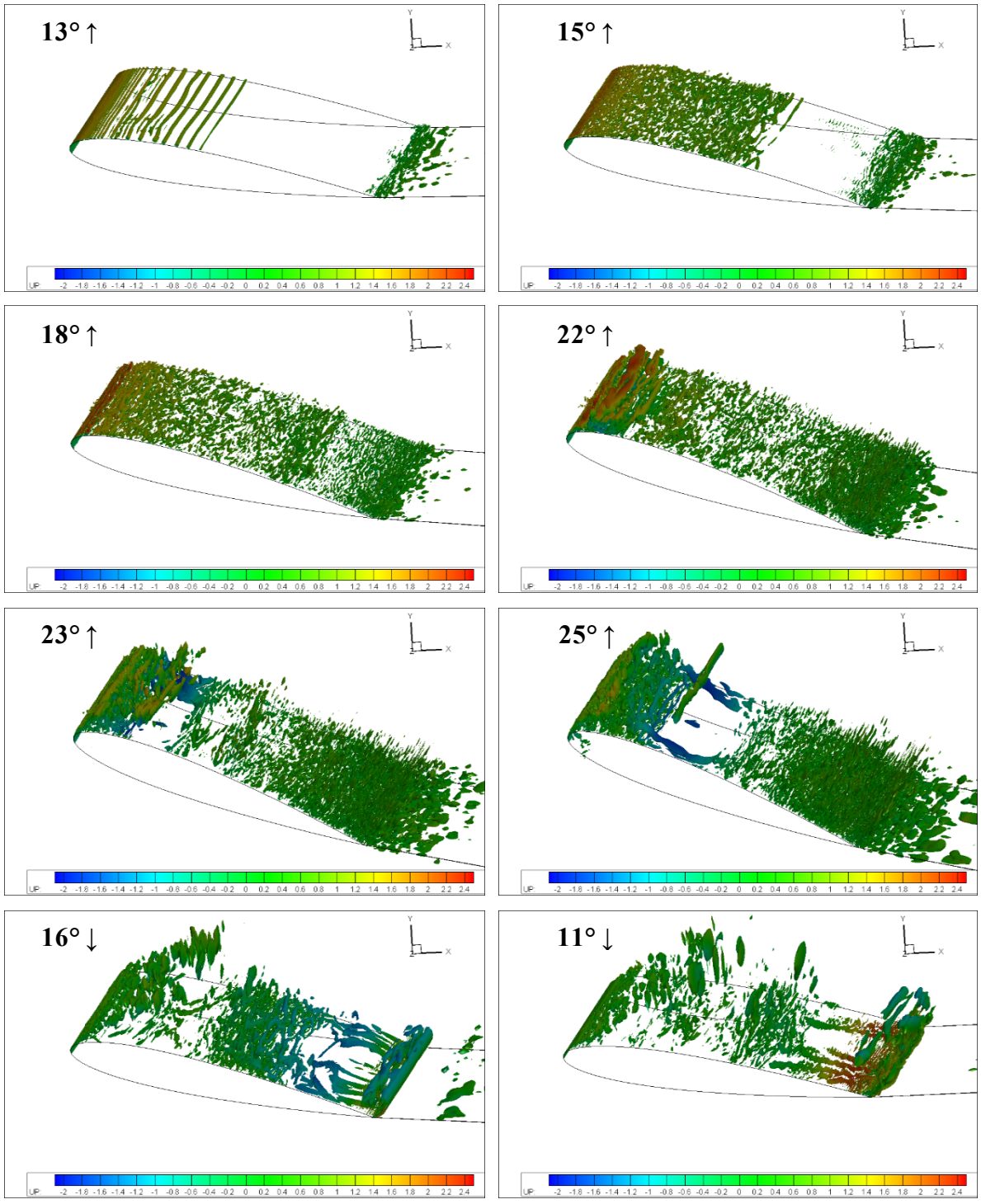

Figure 4-8 Iso-surfaces of Q-criterion colored by streamwise velocity for selected angles (Grid N_z=66).

4.4 2D Simulations

For 2D simulations, lift and drag coefficients were plotted at the left and right axis, respectively, as shown in Figure 4-9. The parameters set in 3D simulations were kept unchanged. Overall, an almost similar trend is observed for all cycles. The pitching airfoil for $\alpha(t) = 10° + 15°\sin(\omega t)$ is classified as deep dynamic stall conditions. Lift and drag coefficients reach the maximum angle of attack before dropping to indicate the stall condition. It is common for the oscillating airfoil to maintain lift and drag force at a higher angle of attack compared to the static condition. This condition persists due to the development of LEV at a higher angle of attack. The LEV can maintain higher lift and drag coefficients at a higher angle of attack before it falls at the beginning of the downstroke phase. The stall happens once the LEV detaches from the airfoil surface.

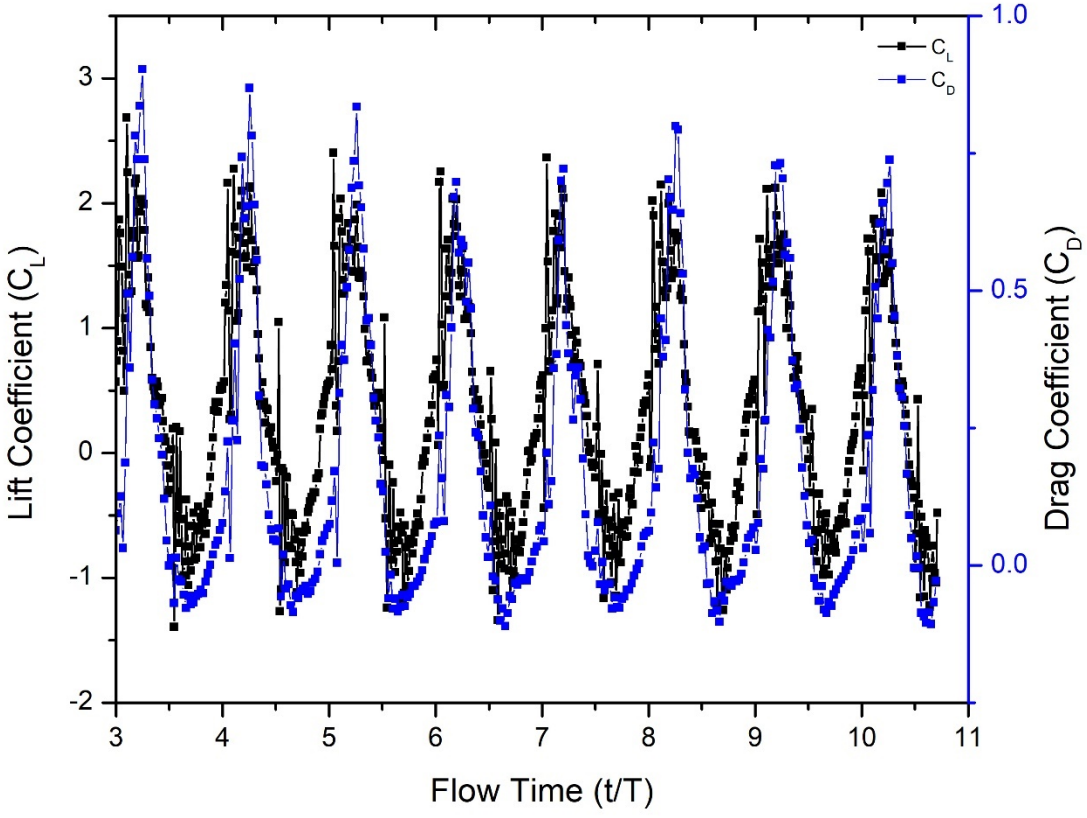

Figure 4-9 History of lift and drag coefficient

Figure 4-10 shows instantaneous streamwise velocity contour for selected angles of attack. At the low angle of attack (i.e. 10.5°), an attached laminar flow is observed around the airfoil surface except in the small trailing edge region. This observation was also discussed in the experiments of Lee and Gerontakos [10]. The development of the energy-containing vortex (LEV) around the leading edge is first seen at 15.8°. This vortex increases in size as the angle of attack increases. Subsequently, this LEV sheds around the suction side of the airfoil and forms an extra suction region that contributes to the increments of lift and causes the delay of the stall angle [41]. At 25°, the formation of the LEV becomes larger, and subsequently, the lift drops. This larger vortex is shedding downstream and interacts with a counter-clockwise vortex known as Trailing-edge Vortex (TEV) and finally sheds to the wake region.

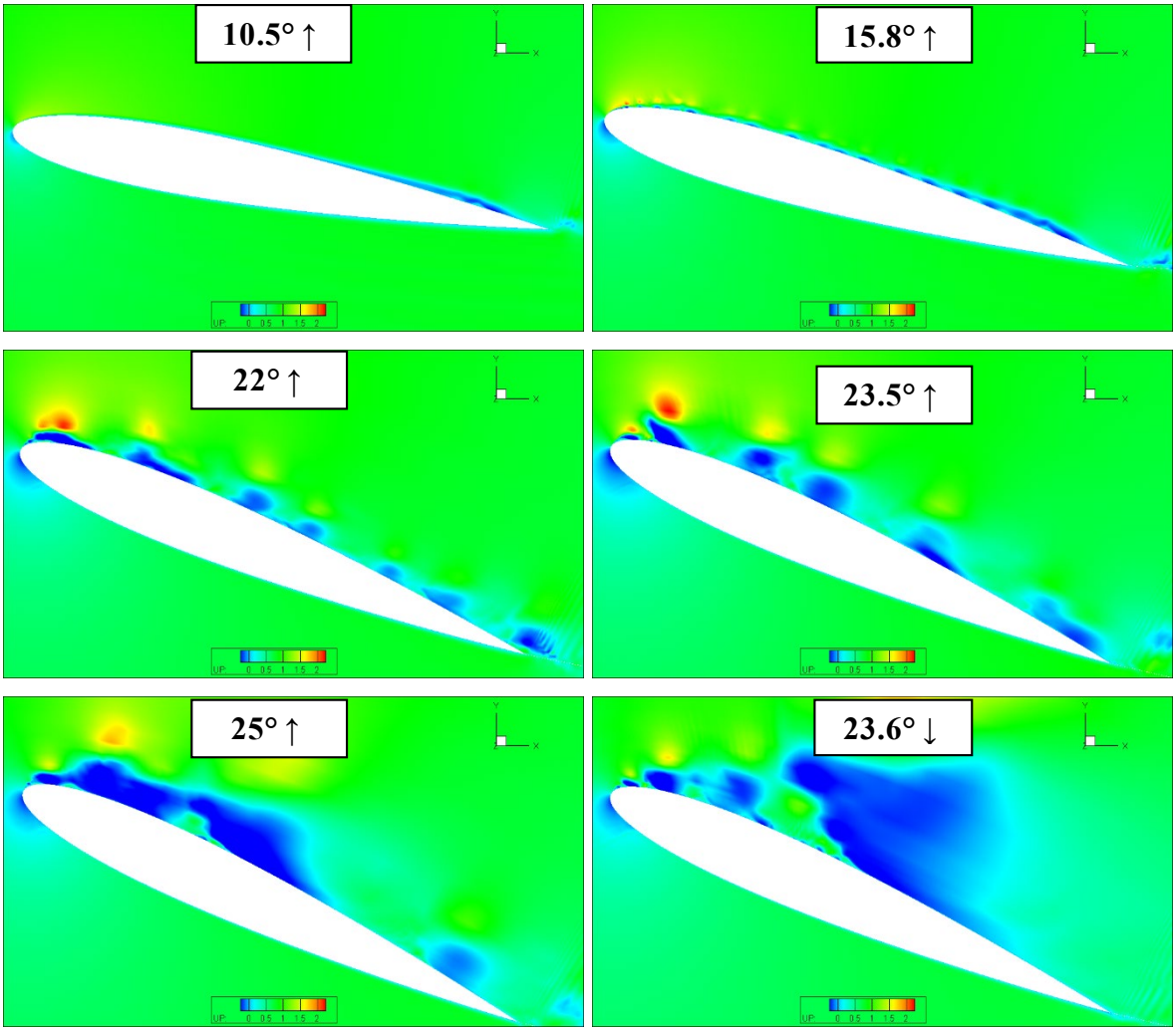

Figure 4-10 Instantaneous Streamwise velocity contour (↑ for upstroke and ↓ downstroke).

Interaction of the TEV can be illustrated based on the vorticity $\omega_Z C/U_\infty$. Figure 4-11 shows the formation of TEV after the dynamic stall at the peak angle of attack 25°. The TEV forms as a counter-clockwise rotating vortex, which appears as the source of circulation [13]. The size of TEV becomes bigger as the airfoil moves in the downstroke phase and combines with the LEV; as a result, the aerodynamics load decreases. The effects of k_{SGS} appear in the formation of TEV. This can be seen in Figure 4-12.

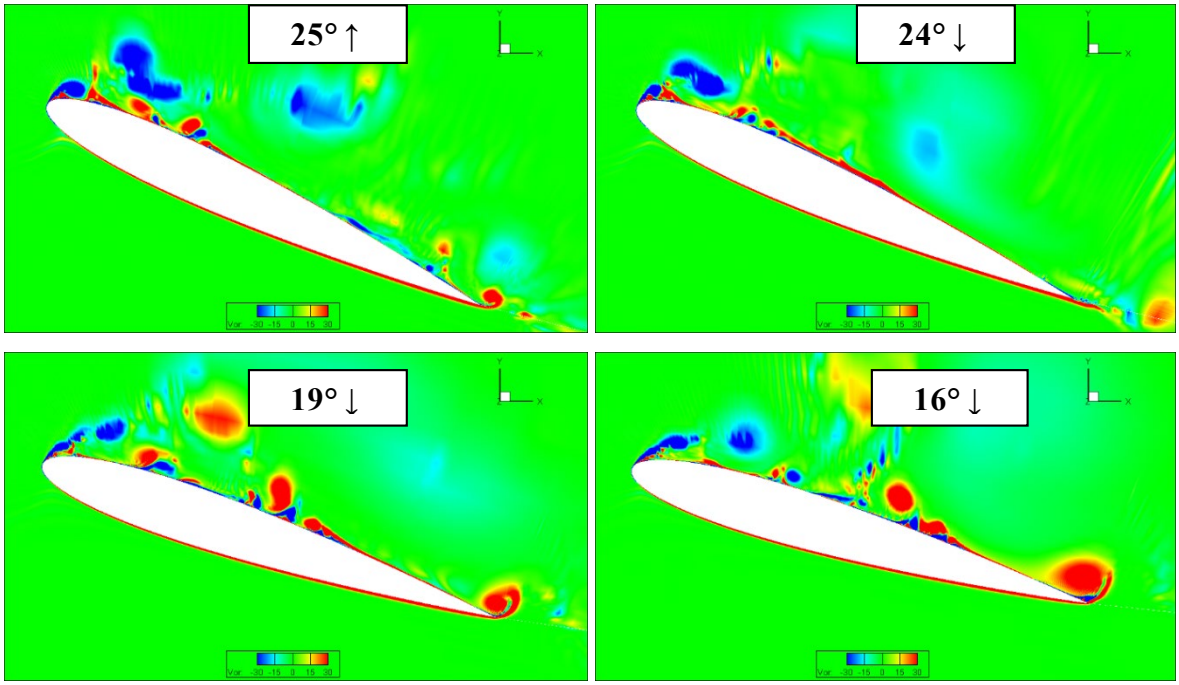

Figure 4-11 Instantaneous vorticity field for oscillating airfoil for selected upstroke and downstroke motion.

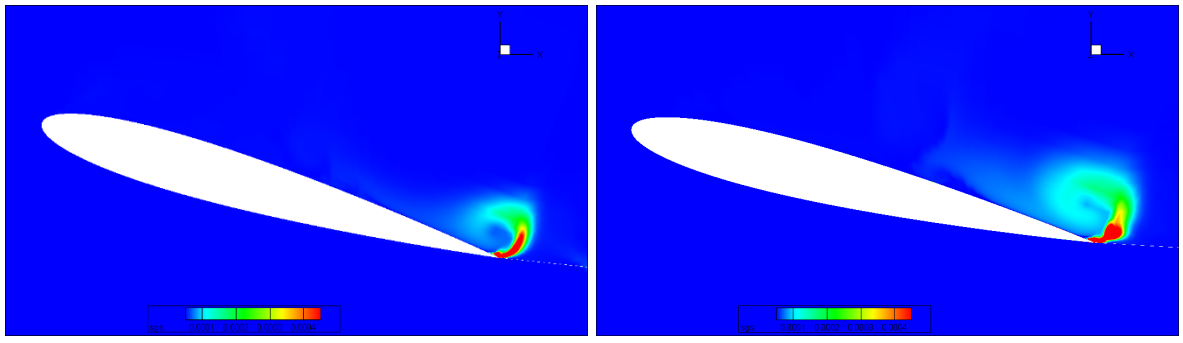

Figure 4-12 Instantaneous SGS energy, k_{SGS} captured information of TEV

4.5 Concluding Remarks

In this chapter, the OD model was applied to unsteady pitching NACA0012 airfoil, and it was revealed that all the essential flow phenomena such as the laminar separation bubble (LSB), leading-edge vortex (LEV), vortex shedding, dynamic stall vortex (DSV), and trailing-edge vortex (TEV) were observed. The angles of LSB and LEV onsets were 15.3° and 20° respectively, and these angles were also reported in the experimental and numerical studies. Plots of pressure coefficient confirmed the existence of a separation bubble where the pressure plateau was detected. Therefore, the results from this chapter revealed that the OD model was able to predict a wide variety of flow phenomena with practical grid points and without any additional transition model.

CHAPTER 5

Conclusion

In this study, it has been intended to develop a practical method of the large-eddy simulation (LES) especially for the analysis of flow around an airfoil in unsteady motion. The SGS kinetic energy one-equation (OD) model was used where the dynamic procedure was applied to determine the coefficient in the production term. The production term was solved by utilizing the dynamic Smagorinsky model (DSM), where the coefficient in the Smagorinsky model (SM) was calculated dynamically. In the SM, the norm of the rate-of-strain tensor and the filter width length is non-zero; therefore, the only possible way to eliminate the eddy viscosity in the non-turbulent region depends on the coefficient. By adopting the dynamic procedure, the coefficient was calculated locally and instantaneously, and the Germano's identity in the dynamic procedure was responsible to filter the turbulent scales in between grid and test filter. The eddy viscosity in the filtered equation of motion was solved indirectly based on the turbulent kinetic energy of SGS, k_{SGS}. Therefore, the production and dissipation terms are not locally equilibrium. The major outcomes of this study are summarized as follows:

- In chapter 1, the current method to predict the laminar-transition region was reviewed, and a special treatment to vanish the eddy viscosity was pointed out to solve that issue. For unsteady pitching airfoil, the transition model was required to predict the LSB.
- In chapter 2, the one-equation k_{SGS} model was shown, and each term in the transport equation was explained. The idea of calculating the production term based on the DSM was emphasized. Owing to these formulations, it could deal with the nonequilibrium feature of spatially developing flow and two-way energy transfer between resolved and SGS portions.

- In chapter 3, the OD model was used to predict the laminar-transitional flows over A-profile airfoil, and it was discovered that no k_{SGS} was reproduced in the laminar region. The transition point was found in good agreement with the experimental data.
- In chapter 4, the OD model was applied to predict the phenomena of deep dynamic stall around unsteady pitching NACA0012 airfoil, and it was revealed that the OD model could produce the laminar separation bubble (LSB), leading-edge vortex (LEV), dynamic stall vortex (DSV), and trailing-edge vortex (TEV) with current grid points. The formation of the LSB and LEV was around 15° and 20°, respectively, and these angles were found in good agreement with the experimental observation.

The result of this study revealed that the OD model was able to predict a wide variety of flow physics involved in static and dynamic stalls without any additional transition model and with practical computational capacity. This model can be further expanded for various engineering applications such as turbomachinery and aeronautics.

APPENDIX A

Derivation of Navier-Stokes Equations (NSE) in Non-Inertial System

The notation vector used for the derivation is elaborated in this chapter.

$\boldsymbol{e}_i (i = 1,2,3)$ is a basis vector in a stationary system.

$\boldsymbol{e}^*{}_i (i = 1,2,3)$ is a basis vector in a non-inertial system.

For the coordinate system, (x_1, x_2, x_3) and (x'_1, x'_2, x'_3) are coordinate systems for the inertial and non-inertial system, respectively.

$$e_i = \frac{\partial x_i}{\partial x_j} e^*{}_j = \frac{\partial x'_j}{\partial x_i} e^*{}_j \qquad A\text{- }1$$

$$e^*{}_i = \frac{\partial x'_i}{\partial x_j} e_j = \frac{\partial x_j}{\partial x'_i} e_j \qquad A\text{- }2$$

Equation A- 1 and A- 2 are basis vectors for the inertial and non-inertial terms. These equations are orthogonal where

$$\frac{\partial x'_i}{\partial x_p} \frac{\partial x'_j}{\partial x_p} = \delta_{ij} \qquad A\text{- }3$$

and any vector **a,** $a = a_i \boldsymbol{e}_i = a'_i \boldsymbol{e}'_i$ .The transformation rule is defined as

$$a_i = \frac{\partial x_i}{\partial x_j} a^*{}_j = \frac{\partial x'_j}{\partial x_i} a^*{}_j \qquad A\text{- }4$$

$$a^*{}_i = \frac{\partial x'_i}{\partial x_j} a_j = \frac{\partial x_j}{\partial x'_i} a_j \qquad A\text{- }5$$

The product of 2 vectors (i.e., $a = a_i \boldsymbol{e}_i = a^*{}_i \boldsymbol{e}^*{}_i$, $b = b_i \boldsymbol{e}_i = b^*{}_i \boldsymbol{e}^*{}_i$)

$$\boldsymbol{a} \times \boldsymbol{b} = \epsilon_{ijk} a_j b_k e_i = \epsilon_{ijk} a^*{}_j b^*{}_k \boldsymbol{e}^*{}_i \qquad A\text{- }6$$

where ϵ_{ijk} is Levi-Civita's alternating tensor. The translational velocity of the non-inertial system is represented by $\boldsymbol{U} = U_i \boldsymbol{e}_i = U^*{}_i \boldsymbol{e}^*{}_i$, while the rotational speed is represented by $\boldsymbol{\Omega} = \Omega_i \boldsymbol{e}_i = \Omega^*{}_i \boldsymbol{e}^*{}_i$.

The time derivative of the basis vector in a non-inertial system is defined as

$$\frac{de^*{}_i}{dt} = \frac{de^*{}_i}{dt'} = \Omega \times e^*{}_i. \qquad A\text{-}7$$

Coordinate transformation on the filtered incompressible NSE has been performed where

$$\frac{\partial \bar{u}_i}{\partial x_i} = 0 \qquad A\text{-}8$$

$$\frac{\partial \bar{u}_i}{\partial t} + \frac{\partial}{\partial x_j}(\bar{u}_i \bar{u}_j) = -\frac{1}{\rho}\frac{\partial \bar{P}}{\partial x_i} + \nu \frac{\partial^2 \bar{u}_i}{\partial x_j \partial x_j} - \frac{\partial \tau_{ij}}{\partial x_j}. \qquad A\text{-}9$$

Performing coordinate transformation on eq. A- 8 and A- 9 yields

$$\frac{\partial \bar{u}_i}{\partial x_i} = \frac{\partial x'_j}{\partial x_i}\frac{\partial \bar{u}_i}{\partial x'_j} = \frac{\partial}{\partial x'_j}\left(\frac{\partial x'_j}{\partial x_i}\bar{u}_i\right) = \frac{\partial \overline{u^*}_i}{\partial x'_i} = \frac{\partial \overline{u^*}_j}{\partial x'_j} \qquad A\text{-}10$$

$$\frac{\partial(\bar{u}_i \bar{u}_j)}{\partial x_j} = \frac{\partial(\overline{u^*}_i \bar{u}_j)}{\partial x_j} = \frac{\partial x'_l}{\partial x_j}\frac{\partial \overline{u^*}_i \bar{u}_j}{\partial x'_l} = \frac{\partial}{\partial x'_l}\left(\overline{u^*}_i \frac{\partial x'_l}{\partial x_j}\bar{u}_j\right) = \frac{\partial \overline{u^*}_i \overline{u^*}_l}{\partial x'_l} \qquad A\text{-}11$$

$$\frac{\partial \bar{P}}{\partial x_i} = \frac{\partial x'_j}{\partial x_i}\frac{\partial \bar{P}}{\partial x'_j} = \frac{\partial \bar{P}}{\partial x'_i} = \frac{\partial \bar{P}}{\partial x'_j} \qquad A\text{-}12$$

$$\frac{\partial^2 \bar{u}_i}{\partial x_j \partial x_j} = \frac{\partial^2 \overline{u^*}_i}{\partial x_j \partial x_j} = \frac{\partial x'_l}{\partial x_j}\frac{\partial x'_k}{\partial x_j}\left(\frac{\partial^2 \overline{u^*}_i}{\partial x'_l \partial x'_k}\right) = \delta_{lk}\left(\frac{\partial^2 \overline{u^*}_i}{\partial x'_l \partial x'_k}\right) = \frac{\partial^2 \overline{u^*}_i}{\partial x'_j \partial x'_j} \qquad A\text{-}13$$

$$\frac{\partial \tau_{ij}}{\partial x_i} = \frac{\partial x'_j}{\partial x_i}\frac{\partial \tau_{ij}}{\partial x'_j} = \frac{\partial \tau_{ij}}{\partial x'_i} = \frac{\partial \tau_{ij}}{\partial x'_j} \qquad A\text{-}14$$

Relative velocity component of fluid in non-inertial system for rotating frame of reference is defined as

$$\bar{u} = \overline{u^*}_i \boldsymbol{e}^*{}_i + \epsilon_{ijk}\Omega^*{}_i \boldsymbol{x'_k} \boldsymbol{e}^*{}_i \qquad A\text{-}15$$

where $\bar{u} = \bar{u}_i e_i = \overline{u^*}_i \boldsymbol{e}^*{}_i$ is the relative velocity of the fluid seen in a non-inertial system. By using eq. A- 16 and transforming the continuity and momentum equation yield

$$\frac{\partial \overline{u^*}_i}{\partial x'_i} + \frac{\partial(\epsilon_{ijk}\Omega^*{}_i x'_k)}{\partial x'_i} = 0 \qquad \text{A- 16}$$

$$\frac{\partial \overline{u^*}_i}{\partial x'_i} = 0 \qquad \text{A- 17}$$

$$\frac{\partial \bar{u}_i}{\partial t} e_i = \frac{\partial \overline{u^*}_i}{\partial t} e^*{}_i + \overline{u^*}_i \frac{\partial e^*{}_i}{\partial t} + \frac{\partial\left(\epsilon_{ijk}\Omega^*{}_i x'_k\right)}{\partial t} e^*{}_i + \epsilon_{ijk}\Omega^*{}_i x'_k \frac{\partial e^*{}_i}{\partial t} \qquad \text{A- 18}$$

$$= \frac{\partial \overline{u^*}_i}{\partial t} e^*{}_i + \overline{u^*}_i \Omega \times e^*{}_i + \frac{\partial\left(\epsilon_{ijk}\Omega^*{}_i x'_k\right)}{\partial t} e^*{}_i + \epsilon_{ijk}\Omega^*{}_i x'_k \Omega \times e^*{}_i$$

By using eq. A- 6, the time derivative term in eq. A- 19 can be transformed into

$$\frac{\partial \bar{u}_i}{\partial t} e_i = \frac{\partial \overline{u^*}_i}{\partial t} e^*{}_i + \epsilon_{ijk}\Omega^*{}_i \overline{u^*}_i e^*{}_i + \epsilon_{ijk}\frac{\partial(\Omega^*{}_i)}{\partial t'} x'_k e^*{}_i + \epsilon_{ijk}\epsilon_{mnk}\Omega^*{}_j \Omega^*{}_m x'_k e^*{}_i \qquad \text{A- 19}$$

For nonlinear convective term,

$$\begin{aligned} \frac{\partial \overline{u^*}_i \overline{u^*}_l}{\partial x'_l} e^*{}_i &= \frac{\partial \overline{u^*}_i (\overline{u^*}_l + \epsilon_{ijk}\Omega^*{}_j x'_k)}{\partial x'_l} e^*{}_i \\ &= \frac{\partial \overline{u^*}_i \overline{u^*}_l}{\partial x'_l} e^*{}_i + \overline{u^*}_l \frac{\partial(\epsilon_{ijk}\Omega^*{}_i x'_k)}{\partial x'_l} e^*{}_i \\ &= \frac{\partial \overline{u^*}_i \overline{u^*}_l}{\partial x'_l} e^*{}_i + \epsilon_{ijk}\Omega^*{}_i \overline{u^*}_k e^*{}_i \end{aligned} \qquad \text{A- 20}$$

For viscosity term,

$$\frac{\partial^2 \overline{u^*}_i}{\partial x'_j \partial x'_j} e^*{}_i = \frac{\partial^2 \overline{u^*}_i}{\partial x'_j \partial x'_j} e^*{}_i. \qquad \text{A- 21}$$

For SGS stress,

$$\frac{\partial \tau_{ij}}{\partial x_i} == \frac{\partial \tau^*{}_{ij}}{\partial x'_i}. \qquad \text{A- 22}$$

Finally, substituting the time derivative term, convective, pressure, viscous term, and SGS stress tensor to form the NSE in a non-inertial system

A- 23

$$\frac{\partial \overline{u^*}_i}{\partial t} e^*{}_i + \frac{\partial \overline{u^*}_i \overline{u^*}_j}{\partial x'_j} \boldsymbol{e}^*{}_i + \frac{\partial \left(\epsilon_{ijk} \Omega^*{}_i \boldsymbol{x'_k}\right)}{\partial t} e^*{}_i + 2\epsilon_{ijk} \Omega^*{}_i \overline{u^*}_k \boldsymbol{e}^*{}_i + \epsilon_{ijk} \epsilon_{mnk} \Omega^*{}_j \Omega^*{}_m \boldsymbol{x'_k} e^*{}_i = -\frac{\partial \bar{P}}{\partial x'_j} \boldsymbol{e}^*{}_i + \nu \frac{\partial^2 \overline{u^*}_i}{\partial x'_j \partial x'_j} \boldsymbol{e}^*{}_i - \frac{\partial \tau^*{}_{ij}}{\partial x'_i}$$

which includes the angular acceleration force, the Coriolis force, and the centrifugal force. Equation A- 23 can be rearranged by combining the Coriolis force into the nonlinear convective term where

A- 24

$$\epsilon_{ijk} \Omega^*{}_i \overline{u^*}_k \boldsymbol{e}^*{}_i = \frac{\partial \epsilon_{ijk} \Omega^*{}_i x'_n \overline{u^*}_j}{\partial x'_j} \boldsymbol{e}^*{}_i,$$

and the final form of NSE in a non-inertial system is defined as

A- 25

$$\frac{\partial \overline{u^*}_i}{\partial t} e^*{}_i + \frac{\partial (\overline{u^*}_i + 2\epsilon_{ijk} \Omega^*{}_i x'_n) \overline{u^*}_j}{\partial x'_j} \boldsymbol{e}^*{}_i + \epsilon_{ijk} \frac{\partial (\Omega^*{}_i)}{\partial t} \boldsymbol{x'_k} e^*{}_i + \epsilon_{ijk} \epsilon_{mnk} \Omega^*{}_j \Omega^*{}_m \boldsymbol{x'_k} e^*{}_i = -\frac{\partial \bar{P}}{\partial x'_j} \boldsymbol{e}^*{}_i + \nu \frac{\partial^2 \overline{u^*}_i}{\partial x'_j \partial x'_j} \boldsymbol{e}^*{}_i - \frac{\partial \tau^*{}_{ij}}{\partial x'_i}$$

REFERENCES

[1] I. Mary and P. Sagaut, "Large Eddy Simulation of Flow around an Airfoil near Stall," *AIAA J.*, vol. 40, no. 6, pp. 1139–1145, 2002.

[2] K. Asada and S. Kawai, "Revisiting LESFOIL: Wall-resolved LES of Flow around an Airfoil at Rec = 2.1 × 10^6," *2018 AIAA Aerosp. Sci. Meet.*, no. January, pp. 1–18, 2018.

[3] S. Dahlstrom and L. Davidson, "Large Eddy Simulation of the Flow around an Airfoil," *39th Aerosp. Sci. Meet. Exhib. Aerosp. Sci. Meet.*, no. January, pp. 1–12, 2001.

[4] S. Dahlström and L. Davidson, "Large Eddy Simulation Applied to a High-Reynolds Flow around an Airfoil Close to Stall," *41st Aerosp. Sci. Meet. Exhib.*, no. January, pp. 1–11, 2003.

[5] M. Germano, U. Piomelli, P. Moin, and W. H. Cabot, "A Dynamic Subgrid-scale Eddy Viscosity Model," *Phys. Fluids A*, vol. 3, no. 7, pp. 1760–1765, 1991.

[6] D. K. Lilly, "A Proposed Modification of the Germano subgrid-scale Closure Method," *Phys. Fluids A*, vol. 4, no. 3, pp. 633–635, 1992.

[7] S. Ghosal, T. S. Lund, P. Moin, and K. Akselvoll, "A Dynamic Localization Model for Large Eddy Simulation," *J. Fluid Mech.*, vol. 286, pp. 229–255, 1995.

[8] G. Martinat, M. Braza, Y. Hoarau, and G. Harran, "Turbulence Modelling of the Flow Past a Pitching NACA0012 Airfoil at 10^5 and 10^6 Reynolds Numbers," *J. Fluids Struct.*, vol. 24, no. 8, pp. 1294–1303, 2008.

[9] W. J. McCroskey, L. W. Carr, and K. W. McAlister, "Dynamic Stall Experiments on Oscillating Airfoils," *AIAA J.*, vol. 14, no. 1, pp. 57–63, 2008.

[10] T. Lee and P. Gerontakos, "Investigation of Flow Over an Oscillating Airfoil," *J. Fluid Mech.*, vol. 512, pp. 313–341, 2004.

[11] M. R. Visbal and S. I. Benton, "Exploration of High-Frequency Control of Dynamic Stall Using Large-Eddy Simulations," *AIAA J.*, vol. 56, no. 8, pp. 2974–2991, 2018.

[12] M. R. Visbal and D. J. Garmann, "Analysis of Dynamic Stall on a Pitching Airfoil Using High-Fidelity Large-Eddy Simulations," *AIAA J.*, vol. 56, no. 1, pp. 46–63, 2017.

[13] K. Gharali and D. A. Johnson, "Dynamic Stall Simulation of a Pitching Airfoil under Unsteady Freestream Velocity," *J. Fluids Struct.*, vol. 42, pp. 228–244, Oct. 2013.

[14] J. A. Ekaterinaris and F. R. Menter, "Computation of Oscillating Airfoil Flows with One- and Two-Equation Turbulence Models," *AIAA J.*, vol. 32, no. 12, pp. 2359–2365, Dec. 1994.

[15] M. R. Visbal and D. J. Garmann, "Investigation of Spanwise End Effects on Dynamic Stall of a Pitching Wing Section," *J. Aircr.*, pp. 1–13, 2019.

[16] S. I. Benton and M. R. Visbal, "Extending the Reynolds Number Range of High-frequency Control of Dynamic Stall," *AIAA J.*, vol. 57, no. 7, pp. 2675–2681, 2019.

[17] M. R. Visbal, "Analysis of the Onset of Dynamic Stall using High-fidelity Large-Eddy Simulations," *52nd Aerosp. Sci. Meet.*, no. January, pp. 1–25, 2014.

[18] M. Dindart and U. Kaynak, "Effect of Turbulence Modeling on Dynamic Stall of a NACA0012 Airfoil," in *30th Aerospace Sciences Meeting & Exhibit*, pp. 1–14.

[19] J. Mukai, S. Enomoto, and T. Aoyama, "Large-Eddy Simulation of Natural Low-frequency Flow Oscillations on an Airfoil near Stall," *Collect. Tech. Pap. - 44th AIAA Aerosp. Sci. Meet.*, vol. 22, no. January, pp. 17066–17075, 2006.

[20] J. H. Almutairi and I. M. AlQadi, "Large-Eddy Simulation of Natural Low-Frequency Oscillations of Separating–Reattaching Flow Near Stall Conditions," *AIAA J.*, vol. 51, no. 4, pp. 981–991, Apr. 2013.

[21] N. Guillaud, G. Balarac, and E. Goncalvès, "LES on a Pitching Airfoil: Analysis of the Lift Coefficient Unsteadiness," *Notes Numer. Fluid Mech. Multidiscip. Des.*, vol. 135, pp. 163–169, 2018.

[22] J. H. Almutairi, L. E. Jones, and N. D. Sandham, "Intermittent bursting of a laminar separation bubble on an airfoil," *AIAA J.*, vol. 48, no. 2, pp. 414–426, 2010.

[23] S. Wang, D. B. Ingham, L. Ma, M. Pourkashanian, and Z. Tao, "Turbulence Modeling of Deep Dynamic Stall at relatively Low Reynolds Number," *J. Fluids Struct.*, vol. 33, pp. 191–209, 2012.

[24] Y. Kim and Z. T. Xie, "Modelling the effect of freestream turbulence on dynamic stall of wind turbine blades," *Comput. Fluids*, vol. 129, pp. 53–66, 2016.

[25] A. Yoshizawa, "Eddy-viscosity-type subgrid-scale model with a variable Smagorinsky coefficient and its relationship with the one-equation model in large eddy simulation," *Am. Inst. Phys.*, vol. 3, no. 8, pp. 2007–2009, 2007.

[26] A. Yoshizawa and K. Horiuti, "A Statistically-Derived Subgrid-Scale Kinetic Energy Model for the Large-Eddy Simulation of Turbulent Flows," *J. Phys. Soc. Japan*, vol. 54, no. 8, pp. 2834–2839, 1985.

[27] M. Okamoto and N. Shima, "Investigation for the One-Equation-Type Subgrid Model with Eddy-Viscosity Expression Including the Shear-Damping Effect," *JSME Int. J. Ser. B*, vol. 42, no. 2, pp. 154–161, 1999.

[28] W. P. Jones and B. E. Launder, "The Prediction of Laminarization with a Two-Equation Model of Turbulence," *Int. J. Heat Mass Transf.*, vol. 15, pp. 301–314, 1972.

[29] J. Taghinia, "Sub-grid Scale Modeling in Large Eddy Simulation with Variable Eddy-Viscosity Coefficient," Aalto University School of Engineering, 2015.

[30] J. Taghinia and M. M. Rahman, "Large Eddy Simulation of Round Impinging Jet with

One-equation Subgrid Scale Model," *Int. J. Heat Mass Transf.*, vol. 116, pp. 1250–1259, 2018.

[31] L. Davidson, "Large Eddy Simulation: A Dynamic One-Equation Subgrid Model for Three-Dimensional Recirculating Flow," in *Proceedings of the 11th International Symposium on Turbulent Shear Flow*, 1997, vol. 3, p. 6.

[32] M. Inagaki and K. Abe, "An Improved Anisotropy-Resolving Subgrid-Scale Model for Flows in Laminar–turbulent Transition Region," *Int. J. Heat Fluid Flow*, vol. 64, pp. 137–152, 2017.

[33] L. Davidson, "LES of Recirculating Flow without any Homogeneous Direction: A Dynamic One-Equation Subgrid Model," in *Proceedings of 2nd Int. Symposium on Turbulence Heat and Mass Transfer,* 1997, pp. 481–490.

[34] T. Kajishima and T. Nomachi, "One-Equation Subgrid Scale Model using Dynamic Procedure for the Energy Production," *J. Appl. Mech.*, vol. 73, no. 3, pp. 368–373, 2006.

[35] C. Han and T. Kajishima, "Large Eddy Simulation of Weakly Compressible Turbulent Flows around an Airfoil," *J. Fluid Sci. Technol.*, vol. 9, no. 4, pp. 1–13, 2014.

[36] S. Kawai and K. Asada, "Wall-modeled Large-Eddy Simulation of High Reynolds Number Flow around an Airfoil near Stall Condition," *Comput. Fluids*, vol. 85, pp. 105–113, 2013.

[37] C. P. Mellen, J. Fröhlich, and W. Rodi, "Lessons from the European LESFOIL project on LES of flow around an airfoil," *40th AIAA Aerosp. Sci. Meet. Exhib.*, no. c, 2002.

[38] H. Lu, C. J. Rutland, and L. M. Smith, "A posteriori tests of one-equation les modeling of rotating turbulence," *Int. J. Mod. Phys. C*, vol. 19, no. 12, pp. 1949–1964, 2008.

[39] M. Tsubokura, T. Kobayashi, N. Taniguchi, and T. Kogaki, "Subgrid scale modeling for turbulence in rotating reference frames," *J. Wind Eng. Ind. Aerodyn.*, vol. 81, no. 1–3, pp. 361–375, 1999.

[40] K. D. Squires and U. Piomelli, "Dynamic Modeling of Rotating Turbulence," in *Turbulent Shear Flows 9*, 1995, pp. 71–83.

[41] F. Geng, I. Kalkman, A. S. J. Suiker, and B. Blocken, "Sensitivity Analysis of Airfoil Aerodynamics during Pitching Motion at a Reynolds Number of 1.35×10 5," *J. Wind Eng. Ind. Aerodyn.*, vol. 183, pp. 315–332, Dec. 2018.

[42] X. Li, D. Grecov, Z. Guo, and Z. Hou, "Influence of Unsteady and Kinematic Parameters on Aerodynamic Characteristics of a Pitching Airfoil," *J. Aerosp. Eng.*, vol. 32, no. 1, pp. 1–11, 2019.

[43] M. Sánchez-Rocha, M. Kirtaş, and S. Menon, "Zonal hybrid RANS-LES Method for Static and Oscillating Airfoils and Wings," *Collect. Tech. Pap. - 44th AIAA Aerosp. Sci. Meet.*, vol. 20, no. January, pp. 15211–15231, 2006.

[44] Y. Shida, K. Kuhawahara, K. Ono, and H. Takami, "Computation of Dynamic Stall of a

NACA-0012 Airfoil," *AIAA J.*, vol. 25, no. 3, pp. 408–413, 1987.

[45] H. Liang, X. Wang, L. Zou, and Z. Zong, "Numerical study of two-dimensional heaving airfoils in ground effect," *J. Fluids Struct.*, vol. 48, pp. 188–202, 2014.

[46] J. JEong and F. Hussain, "On the Identification of a Vortex," *J. Fluid Mech.*, vol. 285, no. February, pp. 69–94, 1995.

[47] H. Kobayashi, F. Ham, and X. Wu, "Application of a Local SGS Model based on Coherent Structures to Complex Geometries," *Int. J. Heat Fluid Flow*, vol. 29, no. 3, pp. 640–653, 2008.